

University of São Paulo
Physics Institute

Study of Jet Quenching in Relativistic Heavy-Ion Collisions

Fabio de Moraes Canedo

Supervisor: Prof. Dr. Marcelo G. Munhoz

Dissertation submitted to the Physics Institute of the University of São Paulo in partial fulfillment of the requirements for the degree of Master of Science.

Examining Committee:

Prof. Dr. Marcelo G. Munhoz - Supervisor (IF-USP)

Prof. Dr. Sandra S. Padula (IFT-UNESP)

Prof. Dr. Tiago Nunes (CFM-UFSC)

São Paulo

2020

À Malu

Agradecimentos

Agradeço o meu orientador, Marcelo G. Munhoz, pelo suporte e pelas discussões ao longo desse período. Agradeço também pela paciência com meu estilo caótico de trabalho. Muitas de nossas conversas trouxeram-me grande paz de espírito e conforto para a minha ansiedade. Oxalá continuemos trabalhando juntos por bastante tempo. Agradeço a Jacquelyn Noronha-Hostler e o Jorge Noronha pelas discussões. Agradeço também os membros do HEPIC, em especial Cristiane Jahnke, Geovane Grossi, Henrique Zanolli, Lucas Teixeira e Ricardo Pitta. Vários bugs não teriam sido resolvidos sem as minhas conversas com vocês. Agradeço o Ricardo Romão da Silva pelo apoio também em vários momentos com o SAMPA.

Agradeço aos professores que tive durante a minha vida, que estimularam minha sede por física e por conhecimento em geral. Nossos encontros fizeram de mim uma pessoa melhor. Em especial os professores Jailton Araújo Oliveira e Sérgio Souza. Agradeço os colegas que tive também durante a graduação, em especial a Carol Guandalim e o Victor Gomes Da Costa Lobo.

Agradeço a minha companheira Malu, pelo carinho e amor. Pelos ótimos momentos que tivemos juntos, pelos conselhos que me deu nessa jornada e por suportar minhas presepadas. Agradeço também pelo apoio que me deu na revisão deste trabalho. Agradeço meus pais Vitor e Marcia por tudo. Agradeço também o suporte e amor incondicional que me deram e continuam me dando. Agradeço meus irmãos Felipe e Mikael por suportarem com graça, na maioria das vezes, minhas brincadeiras. Agradeço ao Jacinto, meu salsicho, pelo calor e carinho enquanto redigi esse trabalho. Agradeço os meus grandes amigos Gabriel Zoha e Rayner Ribeiro pelas discussões sobre física, matemática e pela esporádica companhia alcólica.

Enfim, agradeço ao CNPq, pelo auxílio financeiro, sob o processo 132927/2018-7, sem o qual essa dissertação não poderia ter sido realizada.

*In so far as a scientific statement speaks
about reality, it must be falsifiable; and
in so far as it is not falsifiable, it does not
speak about reality.*

Karl Popper

*“One of the symptoms of an approaching
nervous breakdown is the belief that ones
work is terribly important.”*

Bertrand Russell, *The Conquest of
Happiness*

Resumo

Neste trabalho nós investigamos possíveis impactos que o plasma de Quarks e Glúons pode ter nos observáveis de Jatos. Nós escolhemos o JEWEL (Jet Evolution With Energy Loss) para este estudo. Nós acoplamos o JEWEL com o modelo T_RENTo e também com o MC-KLN+vUSPhydro para as simulações. As simulações foram realizadas para colisões chumbo-chumbo a energia $\sqrt{s_{NN}} = 2.76$ TeV para centralidade 0–10%. Nessas condições, observáveis de forma e geometria dos jatos não são modificados pela implementação de uma hidrodinâmica e condições iniciais realistas. Também calculamos o v_2 dos jatos. Neste caso nós concluímos que as condições iniciais também não afetam esse observável. No caso da hidrodinâmica realista, houve uma melhoria na descrição desse observável.

Palavras-chave: Íons Pesados; Plasma de Quarks e Gluons; Hidrodinâmica; Supressão de Jatos; Cromodinâmica Quântica.

Abstract

In this work, we investigate possible impacts that the behavior of the Quark-Gluon Plasma might have on Jet Observables. We choose JEWEL (Jet Evolution With Energy Loss) for this study. We have coupled JEWEL with T_RENTo and also with MC-KLN+vUSPhydro for simulations. The simulations were performed for PbPb collisions at $\sqrt{s_{NN}} = 2.76$ TeV in the 0 – 10% centrality class. We have found that jet shape observables are mainly unchanged by the inclusion of realistic hydrodynamics and initial conditions in these settings. We also made calculations for the jet v_2 . In this case, we have found that initial conditions do not affect this observable. In the case of realistic hydrodynamics, there is an improvement in the description of data.

Keywords: Heavy-Ion; Quark-Gluon Plasma; Hydrodynamics; Quantum Chromodynamics.

Contents

1	Introduction	1
2	Theory	5
2.1	Quantum Chromodynamics	5
2.2	Quark-Gluon Plasma	6
2.2.1	Hydrodynamics of the Quark-Gluon Plasma	9
2.3	Relativistic Heavy-Ion Collisions	11
2.3.1	Initial Conditions	11
2.3.2	Glauber smooth model	12
2.3.3	T _R ENTo	13
2.3.4	MC-KLN	14
2.4	Hydrodynamics	16
2.4.1	Bjorken expansion	16
2.4.2	v-USPhydro	17
2.5	Jet Quenching	18
2.5.1	Jet Evolution With Energy Loss (JEWEL)	18
2.6	Hadronization	21
2.6.1	Lund Model	21
3	Method	23
3.1	The simulation	23
3.2	Jet Algorithms	25
3.2.1	Background subtraction	28
3.3	Jet Observables	30
3.3.1	Girth	30

3.3.2	Dispersion	30
3.3.3	Jet Mass	31
3.3.4	Azimuthal anisotropy v_2	31
3.4	Grid validation	32
4	Results	39
4.1	Experimental Results	39
4.2	JEWEL results	42
4.3	JEWEL with realistic IC	45
4.4	JEWEL with realistic hydro	52
5	Conclusion	57

List of Figures

1.1	QCD phase diagram	2
2.1	Azimuthal anizotropy representation	7
2.2	Schematics of a parton traversing the medium.	8
2.3	Heavy-ion collision scheme	11
2.4	Energy density in arbitrary units for different initial condition models. The energy density is displayed in arbitrary units.	12
2.5	$T_{RENT}o$ reduction thickness.	14
2.6	Hadron description and its evolution equations.	15
2.7	Interference term appearing in radiation stimulated by multiple scattering. . .	20
2.8	Schematics of a quark and an antiquark and the field between them.	22
3.1	Schematics of force lines created by gluon trajectories between quarks.	25
3.2	Collinear safe ilustration	27
3.3	Collinear safe ilustration	27
3.4	Flow diagram for the anti-kt algorithm.	29
3.5	Schematics of path length dependence of jet quenching. The blue arrow represents a longer trajectory for a parton, and therefore has a higher chance of losing more energy then the orange arrow.	32
3.6	Jet p_T for Grid validation.	33
3.7	Grid/Default for jet p_T	33
3.8	Jet Mass for Grid validation.	34
3.9	Grid/Default for jet mass	34
3.10	Jet Girth for Grid validation.	35
3.11	Grid/Default for jet girth	36
3.12	Jet Dispersion for Grid validation.	36

3.13	Grid/Default for jet dispersion	37
4.1	Experimental Jet p_T	40
4.2	Experimental Jet p_T R_{AA}	40
4.3	Experimental Jet v_2	41
4.4	Experimental Girth and p_t^D	42
4.5	p_T^d and g for pp collisions.	43
4.6	Experimental Jet Mass	43
4.7	Hadron R_{AA}	44
4.8	Charged Hadron R_{AA}	44
4.9	JEWEL prediction of R_{AA} for the jet p_t	45
4.10	JEWEL prediction for girth.	46
4.11	JEWEL prediction for mass.	47
4.12	Jet Girth with realistic IC	48
4.13	Jet p_D^T with realistic IC	49
4.14	Jet Mass with realistic IC	50
4.15	Jet v_2 with realistic IC	51
4.16	Jet Girth	53
4.17	Jet p_D^T	54
4.18	Jet Mass	55
4.19	Jet v_2	56

Chapter 1

Introduction

One of the key problems in particle physics today is the understanding of confinement, property of the fundamental particles that interact through the strong force. This property was originally hypothesized to explain the fact that no particles of fractional charge were ever observed in accelerators and cosmic rays experiments and it was a necessity of the quark model[1]. When the quark model was combined with QCD(Quantum Chromodynamics), it became a major puzzle to explain confinement in light of this theory.

Jets are a consequence of confinement. The way they are generated is through the following mechanism. In accelerator experiments, two partons might interact by exchanging a large momentum, a phenomenon known as hard scattering. When this happens and the quarks start to move away, their potential energy starts to grow linearly. This is different from electromagnetism in which the energy falls as r^{-1} . Due to this increase in energy, it eventually becomes favorable for the system to excite a pair of quarks from vacuum[2]. The system evolves into a new pair of color neutral partons, which are closer together. This process occurs iteratively until the resulting pairs don't have enough energy to increase their distance. The result, experimentally, is a spray of particles that hit the detector with similar angles. These are called jets.

The understanding of confinement necessarily requires also the understanding of QCD vacuum properties as was pointed out by T. D. Lee[3]:

To study the question of “vacuum”, we must turn to a different direction, we should investigate some “bulk” phenomena by distributing high energy over a relatively large volume.

The excited state of matter, in which quarks and gluons are not confined, is called Quark-

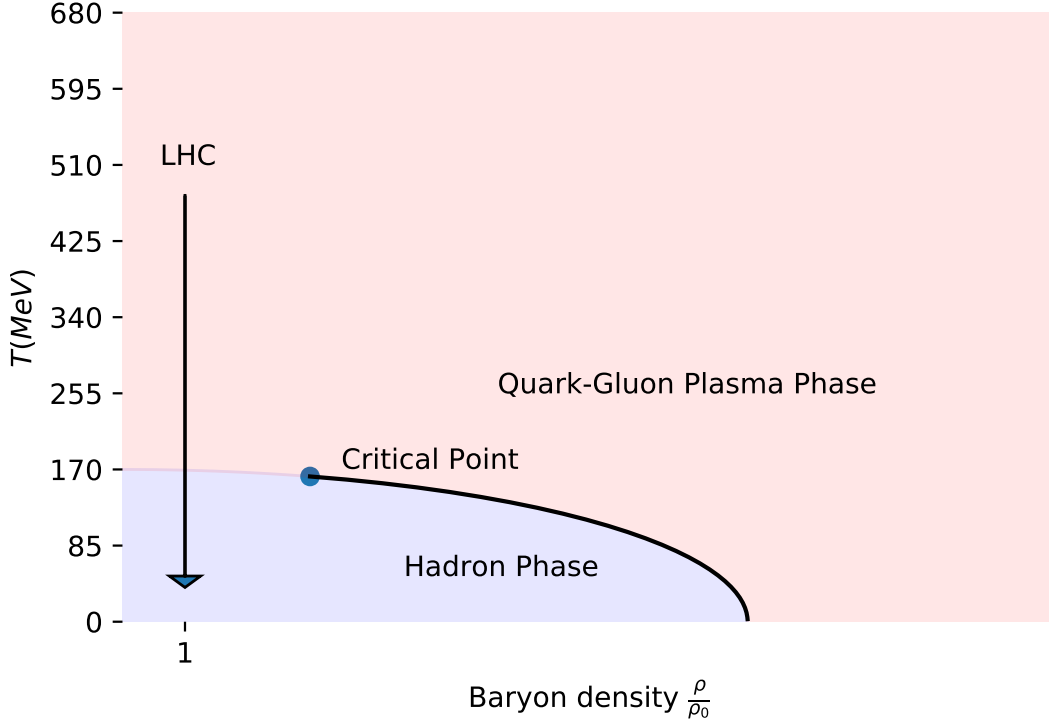


Figure 1.1: QCD phase diagram

Gluon Plasma. This state of matter can be created in the laboratory today through ultra-relativistic heavy-ion collisions. The idea is that during the collision, a good part of the kinetic energy is converted into thermal energy, and a phase transition occurs. Later on, the matter expands and cools down, transitioning back into hadrons, which are bound states of quarks and gluons. These final hadrons eventually stop interacting as well and start their travel as free particles. They potentially go through further decays of electromagnetic or weak nature and then hit the detectors.

Once the particles hit the detector, they might be identified and their properties measured, such as their transverse momentum and their rapidity. The distribution of these particles is then analyzed to try to infer what has happened during the collision. One phenomenon that was identified in the study of this final state is the so-called Jet Quenching. It corresponds to the effects of the medium present in heavy-ion collisions on the hard scattering. When hard scattering occurs in heavy-ion collisions, the partons are surrounded by a color excited medium. Like in an ordinary plasma, a screening effect prevents their potential energy to grow linearly. They interact further with the hot and dense medium created in their surroundings before experiencing the process of jet creation. In this interaction, they lose energy due to

elastic scattering and *gluonstrahlung*, resulting in jets with less energy and broader.

In this work, a study was performed of observables related to Jet Quenching that could be sensitive to the finer details of the initial conditions as well as the hydrodynamic evolution of the quark-gluon plasma formed in ultra-relativistic heavy-ion collisions. Several known observables were analyzed, both from the perspective of the inner jet substructure and shape, as well as soft-high p_T correlation observables such as the jet v_2 . Since that involves collective behavior associated with the soft sector.

In Chapter 2, the theory and the main models used in this work are explained. In Chapter 3, the observables, as well as the techniques used to extract and analyze them are explained. In Chapter 4, the results of the work are presented. In Chapter 5, the conclusions and discussion of the results are presented.

Chapter 2

Theory

2.1 Quantum Chromodynamics

Out of the four known interactions given by the current picture of physics, the one that is of the most importance to this work, is the Strong Force. This force is the one responsible for the nuclear stability. It is described by the following lagrangean density[1, 4]:

$$\mathcal{L}_{\text{QCD}} = -\frac{1}{4}F_{\alpha\beta}^A F_A^{\alpha\beta} + \sum_{\text{flavors}} \bar{q}_A (i\gamma^\mu D_\mu - m)_{AB} q_B \quad (2.1)$$

where $F_A^{\alpha\beta}$ is the gluon field tensor, q_B and \bar{q}_A are the fermion fields and $D_\mu = \partial_\mu + iA_\mu/g$ is the covariant derivative. It describes six fermion fields, corresponding to the known fundamental quarks, and also describes their coupling with a non-abelian Yang-Mills field with the **SU(3)** symmetry. This theory, given its non-abelian nature, has interesting properties that do not appear in electromagnetism.

At first, it is a theory with asymptotic freedom, i.e., the coupling constant decreases as the process under consideration has a larger momentum transfer. This allows one to apply the formalism of perturbation theory in the calculation of high energy processes. Also, it has non-linear terms in the Yang-Mills sector due to the non-commutative nature of the group. These terms describe the field self-interaction, and also make the theory particularly troublesome to allow calculations. They are also responsible for the decrease of the coupling constant aforementioned. As a result, for low energy processes, perturbation theory is no longer reliable. Effective models, semi-analytical and numerical methods, such as lattice QCD, are then used to try to make predictions. These are classified as non-perturbative methods.

As already mentioned, the coupling constant of the theory varies with energy. The behavior of the coupling constant as one varies the energy of a given process was calculated and is given by[2]:

$$\alpha_s(q^2) = \frac{2}{b_0 \ln(-q^2/\Lambda^2)} \quad (2.2)$$

The sign of b_0 in this equation is opposite to that of QED. As a result, the strength of the interaction grows with distance and is unbounded. The scale Λ is a generated scale of QCD and does not depend on quark masses. It is believed that this dynamical scale alone is responsible for the hadron masses, and not the quark masses.

2.2 Quark-Gluon Plasma

The work by E. Fermi[5] and L. Landau[6, 7] on multiparticle production have paved the way for Hagedorn to develop his bootstrap model in the early sixties. There was already an idea to describe particle physics through the formalism of hydrodynamics. For this to be possible, an understanding of the mass spectrum of hadrons was necessary. Hagedorn realized that it was possible to find such a spectrum by understanding that heavy hadrons are bound states of lighter hadrons(which are bound states of lighter hadrons(which are bound states of lighter hadrons(...))). With this idea, he developed a formalism that arrived at the following expression for the mass spectrum:

$$\rho(m) \approx c(m_0^2 + m^2)^{k/2} \exp(m/T_0) \quad (2.3)$$

The parameters were meant to be fixed by experiments. The important consequence of this mass spectrum was that the thermodynamical potentials of a hadron gas would have a singularity as $T \rightarrow T_0$. This was the first indication of a phase transition.

In the eighties[8], with the development of the theoretic understanding of Quantum Chromodynamics, it was predicted that, at a certain temperature, hadrons would “melt” and partons would no longer be confined. This would then induce a phase transition, bringing about a new state of matter, in which quarks and gluons would be the fundamental degrees of freedom of the partition function. Experimental efforts were put forth to create this new state in the laboratory and, by 2005, RHIC had gathered conclusive data that showed this new state of matter had been

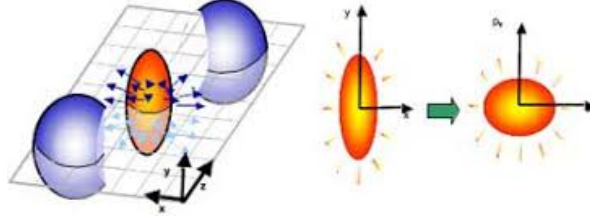


Figure 2.1: Azimuthal anisotropy representation, picture from [10]

created in its experiments[9].

A few signatures of the Quark-Gluon Plasma, name assigned to this new state, were found in these experiments[8]. First, there was the so-called azimuthal anisotropic flow. A phenomenon theoretically explained as the conversion of the asymmetry of the geometric distribution of energy in the transverse plane into an asymmetry in momentum space. Besides, there was the strangeness enhancement of the observed particles, a hint that a possible chemical equilibrium had been achieved during the collisions. There was also the phenomenon of Jet Quenching, commonly explained by the fact that, unlike in proton collisions, the partons generated in the hard scattering must traverse a dense and hot medium. Its main signature was the suppression of high transverse momentum particles.

The azimuthal anisotropic flow, as previously explained, is related to the asymmetry of the collision. It can be better understood by observing Figure 2.1. In the Figure, it is shown that in the interaction region, in orange, there is a preferential direction for the energy deposition. This geometric property of the distribution is called ellipticity. It is responsible for a larger pressure gradient in the x direction. The gradient is the force responsible for the conversion of the asymmetry from the position space into momentum space. The intensity of this conversion can be calculated through hydrodynamic models. This allows the extraction of properties of the Quark-Gluon Plasma, such as its viscosity and EOS(Equation of State).

The strangeness enhancement is explained through the chemical equilibrium that is achieved in heavy-ion collisions[8]. This means that the strange particles are generated through thermodynamical processes, not just in the hard-scattering in the early times of the collision. Also, they are not particles that come from the sea quarks inside the colliding nucleons. Normally, this enhancement is measured by a quantity called R_{AA} , that is defined as the ratio of transverse momentum from pp(proton-proton) to AA(nucleus-nucleus) collisions:

$$R_{AA}(p_T, \eta) = \frac{\frac{dN_{AA}}{dp_T d\eta}}{\langle N_{bin} \rangle \frac{dN_{pp}}{dp_T d\eta}} \quad (2.4)$$

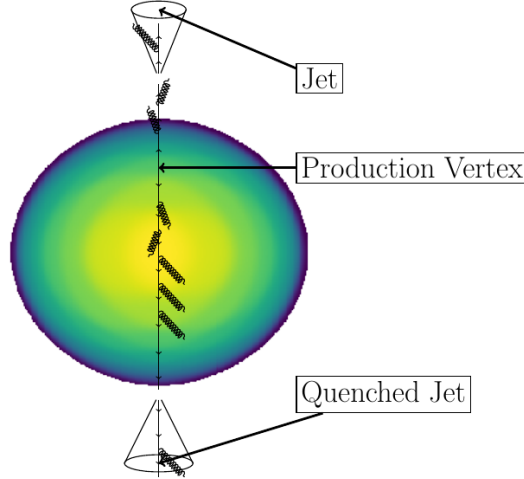


Figure 2.2: Schematics of a parton traversing the medium.

Where N_{AA} is the number of counts (in this case, of strange particles) in AA collisions, N_{pp} is the same count on pp collisions, and $\langle N_{bin} \rangle$ is the average number of binary collisions that happen on a nucleus-nucleus collision, usually estimated with Glauber model.

The Jet Quenching phenomena is observed through the R_{AA} taken from the p_T spectrum of particles. This is theoretically interpreted through the parton energy loss while they traverse the plasma, as illustrated in Figure 2.2. Beyond the spectrum suppression, jet analysis has also revealed that there are distinct fragmentation patterns, as opposed to the vacuum case, hinting a parton-medium interaction[11].

The description of the medium that JEWEL (Jet Evolution With Energy Loss) uses, in its default settings, consists of calculating the partition function by assuming an ideal quantum free gas of non-interacting particles. This model is based on the idea of asymptotic freedom, which is the decrease of the interaction of the partons with the increase of temperature.

This model is necessary to translate temperature profiles into a scattering center density. This is done though the following equation[12, 13]:

$$n_s = 2g_g \zeta(3) \frac{T^3}{2\pi^2} \quad (2.5)$$

Results calculated with the lattice Quantum Chromodynamics approach corroborate that this expressions are valid for $T = 200$ MeV[8]. Before that, at $T \approx 185$ MeV, there is a rapid transition from this fluid to the free hadron gas. These equations for an ideal relativistic quantum gas are used in some Jet Quenching models¹ for the description of the medium.

¹such as JEWEL(Jet Evolution With Energy Loss)

2.2.1 Hydrodynamics of the Quark-Gluon Plasma

Hydrodynamics is the formalism chosen to model the evolution from thermalization until the free streaming of particles. The conversion of hydrodynamic calculations into free hadrons is made with the Cooper-Frye prescription. Hydrodynamics is essentially approached through the relativistic energy-momentum tensor[14]

$$T^{\mu\nu} = \epsilon u^\mu u^\nu + P \Delta^{\mu\nu} \quad (2.6)$$

Where $\Delta^{\mu\nu} = g^{\mu\nu} - u^\mu u^\nu$ is the projection operator orthogonal to u^ν , P is the local pressure and ϵ is the energy density. The conservation equation for this tensor is:

$$\partial_\mu T^{\mu\nu} + \Gamma_{\mu\lambda}^\nu T^{\mu\lambda} = 0 \quad (2.7)$$

This equation has, in total, six independent quantities, four from the local velocity plus two from energy density and pressure. There are four equations from energy-momentum conservation, which leaves two unknowns. The normalization of the four-velocity plus the equation of state then solve the system.

When the system is out of equilibrium, the energy-momentum tensor is different from the one in equation (2.6). In the first order, it assumes the form:

$$T^{\mu\nu} = \epsilon u^\mu u^\nu + P \Delta^{\mu\nu} + \tau^{\mu\nu} \quad (2.8)$$

Where $\tau^{\mu\nu}$ corresponds to a deviation from equilibrium state. This form is constructed by creating an artificial equilibrium state by considering the local energy density, which is a well-defined quantity[15]. Here $\tau^{\mu\nu}$ is required to be symmetric due to the conservation of angular momentum. Also, it is required to satisfy $\tau^{\mu\nu} u_\mu = 0$, according to Landau definition of the four-velocity. Given these properties, $\tau^{\mu\nu}$ can be written as:

$$\tau^{\mu\nu} = \pi^{\mu\nu} + \Pi \Delta^{\mu\nu} \quad (2.9)$$

At this point, it is useful to define the projection operator:

$$\Delta_{\mu\nu}^{\alpha\beta} = \frac{1}{2} \left[\Delta_\mu^\alpha \Delta_\nu^\beta + \Delta_\nu^\alpha \Delta_\mu^\beta - \frac{2}{3} \Delta^{\alpha\beta} \Delta_{\mu\nu} \right] \quad (2.10)$$

It is symmetric in α and β and in μ and ν , and the resulting projection is traceless. This

operator helps us to decompose $\tau^{\mu\nu}$ in two different components with simple physical interpretations.

$$\tau^{\alpha\beta} = \Delta_{\mu\nu}^{\alpha\beta} \pi^{\mu\nu} \quad (2.11a)$$

$$\Pi \Delta^{\alpha\beta} = \pi^{\alpha\beta} - \tau^{\alpha\beta} \quad (2.11b)$$

The first one corresponds to vorticity in the flow, and the second one corresponds to the expansion and compression of the fluid.

The code to integrate numerically the equations (2.7). It will have to be provided with differential equations for the extra degrees of freedom included in $\tau^{\mu\nu}$. This part is usually chosen according to a specific model. The equations used in this work are:

$$\tau_{\Pi}(D\Pi + \Pi\theta) + \Pi + \zeta\theta = 0 \quad (2.12a)$$

$$\tau_{\tau}(\Delta_{\mu\nu\alpha\beta}\tau^{\alpha\beta} + \frac{4}{3}\tau_{\mu\nu}\theta) + \tau^{\mu\nu} = 2\eta\Delta_{\mu\nu\alpha\beta}\Delta^{\alpha}u^{\beta} \quad (2.12b)$$

These are the simplest equations that are both causal and stable. The parameters τ_{Π} and τ_{τ} are lifetimes for the out-of-equilibrium terms. ζ is the bulk viscosity coefficient, and η is the shear viscosity coefficient. θ is the four-divergence of the four-velocity, and $D = u^{\mu}D_{\mu}$, where D_{μ} is the covariant derivative, which, for scalar functions, as is the case in Equation (2.12a), is equal to ∂_{μ} .

Besides the conservation equation (2.7), there might be other currents (Such as baryon number, strangeness number, etc) that satisfy a conservation equation as well:

$$\partial_{\mu}j^{\mu} + \Gamma_{\mu\nu}^{\nu}j^{\mu} = 0 \quad (2.13)$$

Each current included also comes with a conservation equation, so the system is still solvable.

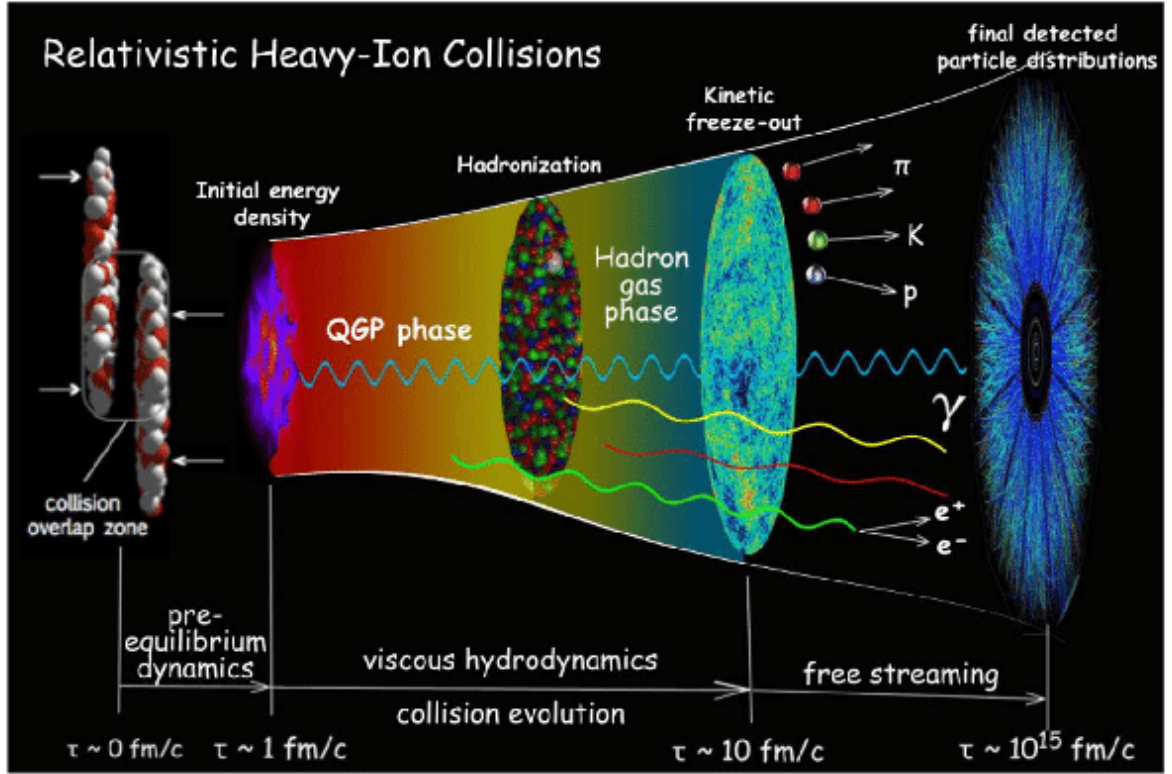


Figure 2.3: Heavy-ion collision scheme, picture from [16]

2.3 Relativistic Heavy-Ion Collisions

The experimental method used to study the QGP is the collision of heavy nuclei at relativistic velocities. The general picture for such a collision can be seen in Figure 2.3. Two Lorentz contracted nuclei approach each other at relativistic speed and then collide, leaving energy in the interaction region. The matter deposited in the interaction region then thermalizes in about $\sim 1 \text{ fm}/c$. This stage is currently the most poorly understood and the source of the largest uncertainty. After thermalization, the hot system expands until $\sim 10 \text{ fm}/c$, a stage that can be simulated with hydrodynamics codes using as input the models that attempt to describe the initial energy density profile. During the hydro evolution, the system reaches the hadronization stage. After the hadron stage the kinetic freeze-out happens in which particles start to stream freely until they reach the detectors at about $\sim 10^{15} \text{ fm}/c$.

2.3.1 Initial Conditions

For the initial conditions, as explained, models are used to predict the energy density profiles that result from the early dynamics of the collision. One of the first models used was

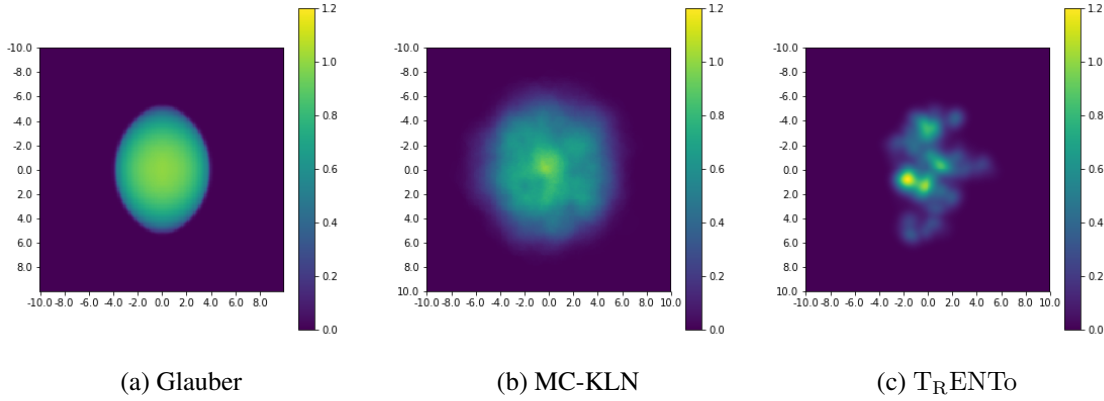


Figure 2.4: Energy density in arbitrary units for different initial condition models. The energy density is displayed in arbitrary units.

Glauber wounded nucleon model[17]. Later, models that implemented sophisticated ideas inspired by QCD were developed. Here we studied three different models. First, we used JEWEL[18, 19] default model, which is a Glauber like without any type of fluctuation in the nucleons positions. Then, we used T_RENTo[20], which is also Glauber inspired, but parametric in nature, and can be tuned to fit certain experimental results and extract qualitative behavior of the initial conditions. And then we used MC-KLN[21], based on the color-glass condensate formalism.

2.3.2 Glauber smooth model

The implementation of the background medium used by JEWEL is an idealized and smooth Glauber model. For nuclei density, a Wood-Saxon distribution is assumed:

$$\rho(\vec{r}) = \frac{1}{1 + \exp(\frac{r-R}{a})} \quad (2.14)$$

Where R is the nuclei radius and a represents a *skin-depth* of the nuclei. This profile density is almost entirely constant for $r < R$. The transverse density is taken from the longitudinal integration:

$$T_A(x, y) = \int dz \frac{1}{1 + \exp(\frac{r(x, y, z) - R}{a})} \quad (2.15)$$

This T_A is called the thickness function. The combination of the thickness function of both nuclei then determines the participant density:

$$n(b, x, y) \propto T_A(x - \frac{b}{2}, y) \left[1 - \exp \left(-\sigma_{NN} T_B(x + \frac{b}{2}, y) \right) \right] + T_B(x + \frac{b}{2}, y) \left[1 - \exp \left(-\sigma_{NN} T_A(x - \frac{b}{2}, y) \right) \right] \quad (2.16)$$

Where σ_{NN} is the nucleon-nucleon cross-section. An example of this participant profile can be observed in Figure 2.4(a). The name smooth used here references the lack of *lumpiness* in this profile, as compared to the others in Figure 2.4.

2.3.3 T_RENTo

T_RENTo[20] is a model for initial conditions for heavy-ion collisions based on the Glauber model. It is based on the idea of the thickness function:

$$T_A(x, y) = \int dz \rho^{\text{part}}(x, y, z) \quad (2.17)$$

Which is built from the density of participants $\rho^{\text{part}}(x, y, z)$. Once the thickness functions of both nuclei are defined, a scalar function is defined as:

$$f = \left(\frac{T_A^p + T_B^p}{2} \right)^{1/p} \quad (2.18)$$

Where p is a free parameter. This is a generalized mean and is taken to be proportional to the entropy deposition. This function has a general behavior that changes continuously with the parameter p , interpolating between maximum and minimum. Each value corresponds to a qualitatively different entropy deposit mechanism. The qualitative behavior of this function can be seen in Figure 2.5.

The participant densities are built by considering pairs of nucleons, one from each nucleus. Their positions are sampled from a Woods-Saxon potential. Then for each pair the probability of collision is taken as:

$$P_{\text{coll}} = 1 - \exp \left[-\sigma_{gg} \int dx dy \int dz \rho_A \int dz \rho_B \right] \quad (2.19)$$

Here we have that σ_{gg} is adjusted so that the total proton cross-section is σ_{NN} [20]. If the nucleons do collide, then the thickness function is built from the sum of each nucleon density, which is taken to be a gaussian. So each nucleon contributes with a thickness function given

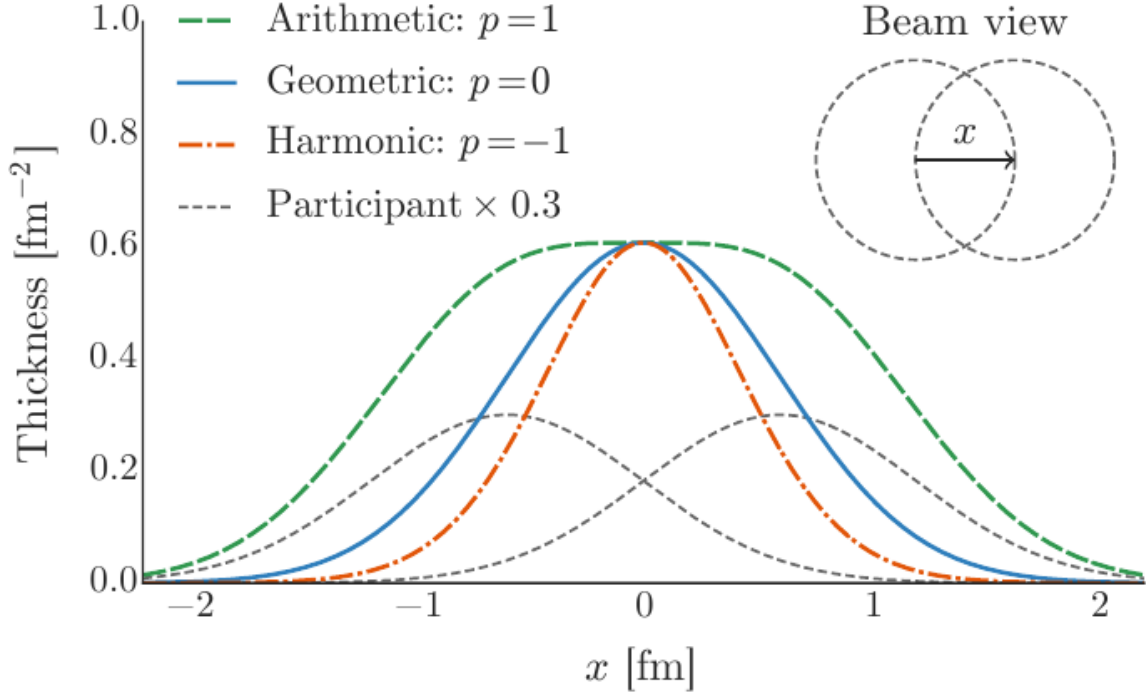


Figure 2.5: T_{RENTTo} reduction thickness. The dashed lines correspond to nucleon profiles and the colored lines correspond to the reduced thickness for different values of p . Picture from [20]

by:

$$T_N = w \int dz \rho_N(x, y, z) \quad (2.20)$$

Where w is a random weight sampled from a gamma distribution with unity mean:

$$P_k(w) = \frac{k^k}{\Gamma(k)} w^{k-1} e^{-kw} \quad (2.21)$$

This creates an extra degree of fluctuation that will be encoded in a parameter k that can be chosen to fit experimental results. An example of a T_{RENTTo} profile for $p = 0$, which is a tune that reproduces IP-Glasma behavior, can be seen in Figure 2.4(c). The effects of fluctuations can be observed in the figure.

2.3.4 MC-KLN

The MC-KLN[21] model is based on the color glass condensate approach. The key idea is that a nuclei is essentially a gluon wall with a wavelength bigger than the contracted longitudinal size of the other nuclei. So the collision occurs in a coherent manner. This comes from the fact

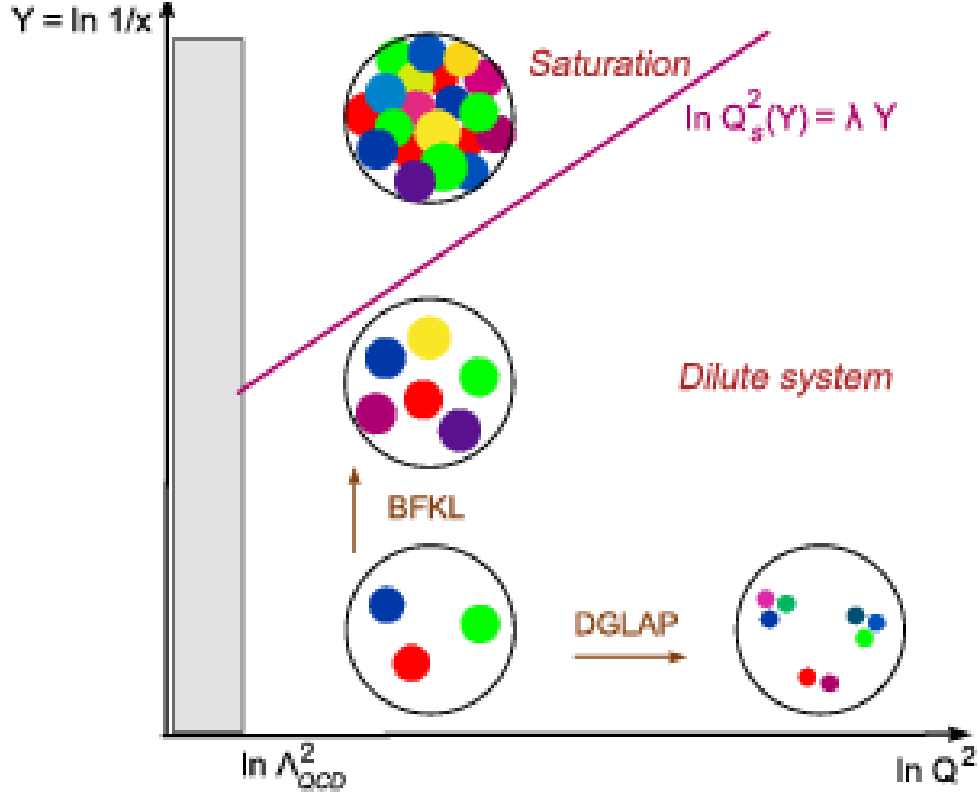


Figure 2.6: Hadron description and its evolution equations.

that a hadron can be seen as a collection of partons and the picture we see varies with x and Q^2 . The description of a hadron with varying these quantities can be seen in Figure 2.6. The quantity x represents the fraction of the hadron energy carried by the partons. The smaller this fraction, then higher is the number of partons. Q^2 can be understood as the transverse momentum carried by each parton, which is negatively correlated with the transverse size of each parton, according to the uncertainty principle. Evolving in x implies then considering the emission of partons by partons, increasing the number of constituents of a hadron. Eventually, though, the cross-section for partons to absorb partons becomes large, and the number of gluons no longer increases.

A saturation scale can be defined such that below it the occupation number of gluons is constant, and above, we have a distribution that obeys the BFKL equations[22]. The saturation scale is defined in terms of the thickness function, according to:

$$Q_{s,A}^2(x, \mathbf{r}_\perp) = 2 \text{ GeV}^2 \left(\frac{T_A(\mathbf{r}_\perp)/p_A(\mathbf{r}_\perp)}{1.53} \right) \left(\frac{0.01}{x} \right)^\lambda \quad (2.22)$$

Where $T_A(\mathbf{r}_\perp)$ is the thickness function and x is the fraction of the momentum carried by the gluon in the distribution. $p_A(\mathbf{r}_\perp)$ is the probability of finding at least nucleon at a given

transverse coordinate. In this way, the model proceeds by randomly picking nucleon positions according to a Woods-Saxon potential, and then it determines the thickness function, finally determining the saturation scales. The gluon distributions are then combined through:

$$\frac{dN_g}{dyd^2\mathbf{r}_\perp} \sim \int \frac{d^2p_\perp}{p_\perp^2} \int d^2k_\perp \phi(n_{part,A})\phi(n_{part,B}) \quad (2.23)$$

where:

$$\phi(x, k_\perp, \mathbf{r}_\perp) \sim \frac{1}{\alpha(Q_s^2)} \frac{Q_s^2}{\max(Q_s^2, k_\perp^2)} \quad (2.24)$$

And ϕ is the gluon distribution function. An example of an MC-KLN generated profile can be seen in Figure 2.4(b). The larger spread of the energy density is a consequence of the tail of the gluon distribution in Equation (2.24). The ansatz in Equation (2.23) comes from considering a number of binary collisions between the gluons and a given position in transverse space.

2.4 Hydrodynamics

The implementation of the hydrodynamics involves developing a numerical method for integration of the hydrodynamic equations, as well as an Equation of State and the differential equations satisfied by the independent components of the $\tau^{\mu\nu}$ tensor. Here we used two ways to model this stage of the collision. First, as the JEWEL default, we used the Bjorken longitudinal expansion model, which is only an approximation. For a more realistic treatment, we used the 2+1 code v-USPhydro.

2.4.1 Bjorken expansion

One of the first models developed to calculate the evolution of the QGP was the one developed by Bjorken that approximates the system to a one-dimensional system and considers the expansion only in the longitudinal direction. This model then predicts a decay of the energy density that can explain the plateau in the rapidity spectrum. The idea is that we have a blast wave in the longitudinal direction that is bound by the speed of sound in the medium:

$$T = T_0 \left(\frac{\tau_0}{\tau} \right)^{v_s^2} \quad (2.25)$$

where τ_0 and T_0 are chosen to fit experimental data, mainly the $\frac{dN}{d\eta}$ observable. Since the

speed of sound is calculated, for a relativistic ideal quantum gas, to be $v_s^2 = \frac{1}{3}$, we have a complete description of the temperature evolution of the system. The values chosen in JEWEL[23] are $\tau_0 = 0.5 \text{ fm}/c$ and $T_0 = 530 \text{ MeV}$.

2.4.2 v-USPhydro

The hydrodynamics model used here is v-USPhydro[24–26]. It utilizes the Lagrangian method to implement the integration of the conservation equations that describes the hydrodynamics. This method consists, as an alternative to the grid methods, of discretizing the fluid density profile into particles and allowing their positions to evolve as well. One of the advantages of this approach is that it can be efficiently applied to unbound systems, as is the case of nuclei collisions. This formalism is called Smoothed Particle Hydrodynamics.

The idea is to use a finite number of cells to describe the fluid. One then defines a normalized kernel:

$$\int W[\mathbf{r}; h] d^2\mathbf{r} = 1 \quad (2.26)$$

where \mathbf{r} is a transverse position coordinate and h is a parameter that plays a similar role to the grid spacing in the Euler method. This kernel can then use the cells to calculate the value of a field at any point in space:

$$\tau\gamma\sigma \rightarrow \sigma^*(\mathbf{r}, \tau) = \sum_{\alpha=1}^{N_{SPH}} \nu_{\alpha} W[\mathbf{r} - \mathbf{r}_{\alpha}(\tau); h] \quad (2.27)$$

Where τ is the proper time, γ is the relativistic factor. σ is the entropy density and N_{SPH} is the number of Smoothed Particle cells. The conservation of $\tau\gamma\sigma$ is then equivalent to:

$$\sum_{\alpha=1}^{N_{SPH}} \nu_{\alpha} = K \quad (2.28)$$

where K is a constant and the ν_{α} are chosen to match an initial distribution. The entities that occupy the positions \mathbf{r}_{α} are referred to as SPH particles. Now, given some extensive quantity associated to the density $a(\mathbf{r}, \tau)$, the discretized version of it will be:

$$a(\mathbf{r}, \tau) = \sum_{\alpha=1}^{N_{SPH}} \nu_{\alpha} \frac{a(\mathbf{r}_{\alpha}(\tau))}{\sigma^*(\mathbf{r}_{\alpha}(\tau))} W[\mathbf{r} - \mathbf{r}_{\alpha}(\tau); h] \quad (2.29)$$

And the derivative of it will be:

$$\frac{d}{d\mathbf{r}}a(\mathbf{r}, \tau) = \sum_{\alpha=1}^{N_{SPH}} \nu_{\alpha} \frac{a(\mathbf{r}_{\alpha}(\tau))}{\sigma^*(\mathbf{r}_{\alpha}(\tau))} \frac{d}{d\mathbf{r}} W[\mathbf{r} - \mathbf{r}_{\alpha}(\tau); h] \quad (2.30)$$

So, a knowledge of the derivative of the kernel function allows one to calculate the derivative of any extensive quantity. Similarly, the proper-time derivative:

$$\frac{d}{d\tau}a(\mathbf{r}, \tau) = \sum_{\alpha=1}^{N_{SPH}} \nu_{\alpha} \frac{a(\mathbf{r}_{\alpha}(\tau))}{\sigma^*(\mathbf{r}_{\alpha}(\tau))} \frac{d\mathbf{r}_{\alpha}(\tau)}{d\tau} \frac{d}{d\mathbf{r}_{\alpha}(\tau)} W[\mathbf{r} - \mathbf{r}_{\alpha}(\tau); h] \quad (2.31)$$

The equations of motion for the fluid are[27, 28]:

$$\gamma \frac{d}{d\tau} \left[\frac{(\epsilon + p + \Pi)}{\sigma} u^{\mu} \right] = \frac{1}{\sigma} \partial^{\mu} (p + \Pi) \quad (2.32a)$$

$$\gamma \frac{d}{d\tau} \left(\frac{s}{\sigma} \right) + \left(\frac{\Pi}{\sigma} \right) \frac{\theta}{T} = 0 \quad (2.32b)$$

$$\tau_{\Pi} \gamma \frac{d}{d\tau} \left(\frac{\Pi}{\sigma} \right) + \frac{\Pi}{\sigma} + \left(\frac{\zeta}{\sigma} \right) \theta = 0 \quad (2.32c)$$

$$\tau_{\tau} \gamma \Delta_{\mu\nu\alpha\beta} \frac{d}{d\tau} \left(\frac{\tau^{\alpha\beta}}{\sigma} \right) + \frac{\tau_{\mu\nu}}{\sigma} = 2 \frac{\eta}{\sigma} \Delta_{\mu\nu\alpha\beta} \nabla^{\alpha} u^{\beta} \quad (2.32d)$$

where ζ and η are the bulk and shear viscosity, ϵ , s and σ are the energy density, the entropy density, and the system density, respectively. T is the temperature and θ is the four divergence of the velocity that describes the expansion rate of the system. The EOS used by v-USPhydro is S95n-v1. The coefficients used for the viscosities are $\frac{\eta}{s} = 0.3$ and $\frac{\zeta}{s} = 0.08$. v-USPhydro integrates these equations using the discretization procedure described above using a Runge-Kutta method and then calculates freeze-out surface and temperature profile and other quantities. For this work, we are interested in the temperature profile.

2.5 Jet Quenching

2.5.1 Jet Evolution With Energy Loss (JEWEL)

JEWEL[18, 23, 29] is a Monte-Carlo implementation of a perturbative formalism, called the BDMPS-Zakharov formalism which treats elastic collisions and radiation for a parton moving in a dense environment. One of the issues that appears when one wants to consider Monte-Carlo

implementations of quantum phenomena is that one must deal with amplitudes, not probabilities. An important consequence of this is the appearance of the so-called QCD LPM (Landau-Pomeranchuk-Migdal) effect. So JEWEL addresses this by the definition of a parameter that will separate the cases where interference might occur. This parameter is called the gluon formation time:

$$\tau = \frac{\mathbf{k}^2}{2\omega} \quad (2.33)$$

Where \mathbf{k} is the radiation momentum, and ω is the radiation energy. This parameter is used to determine if two successive scatterings are within the formation time of an emission. If that is the case, JEWEL treats the scattering centers as coherent sources of the *gluonstrahlung*.

The algorithm implemented in JEWEL is the following. First, a pair of partons is generated through hard scattering in a point in transverse space proportional to the energy-density. This first hard scattering is generated with PYTHIA[30]. Then these partons are propagated through the medium in the transverse plane. In this process they will lose energy through collisions and radiation. After they escape the medium, the event is given back to PYTHIA[30] to perform fragmentation and hadronization.

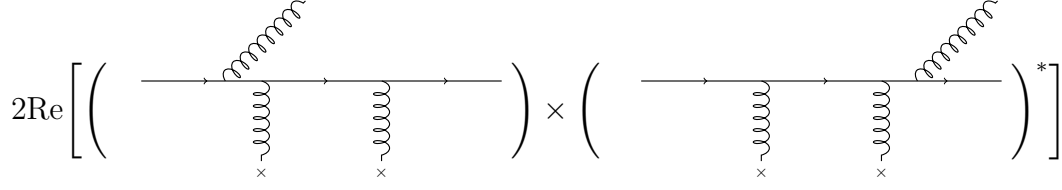
The parton shower is implemented in JEWEL through the virtuality ordering procedures that resums leading logarithm of pQCD. It is implemented through the so-called Sudakov form factor:

$$\mathcal{S}(t_h, t_c) = \exp \left\{ - \int_{t_c}^{t_h} \frac{dt}{t} \int_{z_{\min}}^{z_{\max}} dz \sum_b \frac{\alpha_s(k_{\perp}^2)}{2\pi} \hat{P}_{ba}(z) \right\} \quad (2.34)$$

This can be interpreted as the probability that a parton emits no radiation between the scales t_h and t_c . The function $\hat{P}(z)$ is the so-called Altarelli-Parisi splitting function. This Sudakov form-factor is used to determine the scale of the next splitting in the parton shower. This shower will behave as if it was in vacuum. It is the collisional process that allows for the generation of further virtuality evolution and will be responsible for medium-modifications of the jet.

The collisional part of JEWEL is treated through simple $2 \rightarrow 2$ matrix elements squared. A thermal mass is attributed to the gluons representing the scattering centers. This is the Debye mass given by $\mu_D \approx 3T$. The $2 \rightarrow 2$ cross-section then takes the form:

$$\sigma_i(E, T) = \int d|\hat{t}| \int dx \sum_{j \in \{q, \bar{q}, g\}} f_j^i(x, \hat{t}) \frac{d\hat{\sigma}_j}{d\hat{t}}(x\hat{s}, |\hat{t}|) \quad (2.35)$$

$$2\text{Re} \left[\left(\text{diagram 1} \right) \times \left(\text{diagram 2} \right)^* \right]$$


The figure shows two Feynman diagrams representing interference terms. Each diagram consists of a horizontal line with arrows indicating the direction of particle flow. In the first diagram, a wavy line (representing a gluon) is emitted from the top of the line at a vertex marked with an 'x', and another wavy line is emitted from the bottom of the line at a vertex marked with an 'x'. In the second diagram, the wavy lines are emitted from the bottom and top vertices respectively. The diagrams are enclosed in large parentheses, and the entire expression is multiplied by 2Re and the second term is complex conjugated.

Figure 2.7: Interference term appearing in radiation stimulated by multiple scattering.

Where \hat{s} is the collision energy on the center of mass, $\hat{\sigma}$ is the $2 \rightarrow 2$ scattering cross-section. And $f_j^i(x, \hat{t})$ is the PDF that describes the probability of finding a parton j in a parton i with momentum fraction x at the momentum transfer \hat{t} . The PDF shown in the above equation represents the initial-state radiation emitted by the projectile. This implements higher order effects in the perturbative calculation. In this prescription, Bremsstrahlung is automatically taken into account.

The main difficulty in implementing Monte-Carlo simulations for quantum systems is the fact that quantum systems are not Markov chains. There is always the presence of interference effects that must be taken into account. JEWEL does it so using a parametrically formation time attributed to the radiated gluons from the projectile. If the formation time of emission is longer than two consecutive scatterings, then these cases must be analyzed and dealt with specially.

To summarize, the steps taken by JEWEL are the following:

- 1 First, a hard scattering is generated in PYTHIA, producing the partons to be propagated;
- 2 JEWEL evolves this parton state with collisions and radiation, taking into account the non-abelian Landau-Pomeranchuk-Migdal effect;
- 3 Once the partons are close enough to mass shell and have escaped the medium, the final partonic state is handed back to PYTHIA;
- 4 PYTHIA performs the fragmentation of the partonic final state and hadronization, as well as the resonance decays;

The LPM effect is an effect that enters multiple scattering when the scale of a radiation does not allow one to treat two successive scatterings as independent. Crossed terms in the squared amplitude, such as the one displayed in Figure 2.7, create a destructive interference. To handle it, JEWEL proceeds with a formation time prescription that dictates if the successive scatterings are seen as one by the radiated gluon.

2.6 Hadronization

Jets, as described before, are a natural consequence of confinement. The formation of jets from partons is called hadronization. Unfortunately, hadronization is a low energy process and falls within the realm of non-perturbative Quantum Chromodynamics. As an implication, a lot of models are used to describe this process and not first principle calculations. One such model is the Lund model. This is the model implements by PYTHIA, which was used to convert the final partonic state provided by JEWEL into a set of hadrons.

2.6.1 Lund Model

The Lund string model is based on the idea of tunneling in quantum mechanics. The equation that must be satisfied by the wavefunction of a quark coming out of the Dirac sea is[31]:

$$[(p - A)^2 - m^2] \psi = 0 \quad (2.36)$$

Where p is the particle 4-momentum, A is the four potential and m is the particle mass. The potential between a quark and an antiquark is linear in the z coordinate. Expanding this equation and separating the variables, we can arrive at:

$$\psi = \exp[i(p_x x + p_y y - Et)] f(z) = 0 \quad (2.37)$$

Where $f(x)$ satisfies the equation:

$$\{[E - A_0(z)]^2 - p_z^2 - m_T^2\} f(z) = 0 \quad (2.38)$$

Where $m_T = \sqrt{p_T^2 + m^2}$. Here we have assumed only a scalar potential A_0 [31]. Dividing this equation by m_T we arrive at:

$$\left[\frac{p_z^2}{2m_T} + V_{eff}(z) - E_{eff} \right] f(z) = 0 \quad (2.39)$$

Which is a Schrödinger equation for an effective energy $E_{eff} = 0$ and an effective potential of the form:

$$V_{eff}(z) = \frac{m_T}{2} - \frac{[E - A_0(z)]^2}{2m_T} \quad (2.40)$$

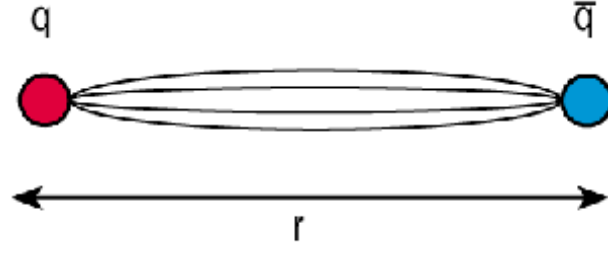


Figure 2.8: Schematics of a quark and an antiquark and the field between them.

We assume the potential to be linear. To see why this is the case, one can look at Figure 2.8. The lines of force do not spread into space. This happens because the gluon field carries charge and it is attracted to itself. The gluon field also satisfies Gauss's law. As a result, the flow in any cross-sectional surface between the quarks must be the same. This implies a constant electric field, which in turn, implies a linear potential:

$$A_0(z) = -\kappa z \quad (2.41)$$

Coupling this formalism with the WKB method, we arrive at[31]:

$$P = \exp \left\{ -\frac{\pi m_T^2}{\kappa} \right\} \quad (2.42)$$

This equation indicates that particles with a greater transverse mass have a lower probability of being produced and explains the hadrochemistry observed in jets. The mechanism just explained is the Schwinger particle production mechanism. It was created to describe pair creation in strong electric fields in QED. It was adapted to the context of QCD where it could describe the behavior of jets, e.g. their multiplicity.

Once the parton pairs no longer have enough energy to break the strings, they become resonances that decay into hadrons in a Lorentz invariant way. At this stage, phase space considerations are used to determine the momenta of the decay products[30].

Chapter 3

Method

3.1 The simulation

The simulation built in this work to study the phenomenon of Jet Quenching is performed by coupling JEWEL with an alternative. A description of the models used in this work can be found in Chapter 2. First, a simulation was performed with the JEWEL using the default settings, which simulates an idealized version of the initial conditions and the medium¹, with the density decaying due to longitudinal expansion only². After that, JEWEL code for the medium was modified with an implementation to read the temperature profiles of an arbitrary model. This allowed us to study the effects of different initial conditions and also a realistic hydrodynamic evolution. For this, a choice was made to create a grid with spacing 0.15 fm on which the temperature profile was read from a foreign model. The time step used is of 0.1 fm/c. This is a time step larger than necessary for hydro simulations, but we are not integrating differential equations, so this does not insert great numerical errors, for more detail refer to the discussion on the last session of this chapter. For intermediate values, a bicubic interpolation was used.

After this procedure, the generated events on JEWEL were analyzed with code developed with the Rivet[32] package for analysis of the generated Monte-Carlo events. FastJet[33] package was also used. The observables generated were the ones in Section 3.2. The uncertainty on the histogram bins presented in Sections 4.3 and 4.4 are calculated for a binomial distribution according to the statistics generated by the Monte-Carlo events. Since there are specific features for this analysis, such as the recoiling scattering centers³, the analysis was built with the

¹see Subsection 2.3.2

²see Subsection 2.4.1

³see Section 3.2.1

Scenarios		
	Initial conditions	Evolution
Default	Ideal	Longitudinal expansion
T _R ENTo	T _R ENTo	
MC-KLN	MC-KLN	
v-USPhydro + MC-KLN	MC-KLN	2+1 v-USPhydro code

Table 3.1: Scenarios simulated in this work. See Charter 2 for explanation on the items of the table.

aforementioned packages to attend our specific needs.

The simulation in each of the cases consists of a thousand of different medium profiles, and ten thousand JEWEL Monte-Carlo events generated for each profile. The different simulated scenarios are displayed in Table 3.1. The analysis was performed in the 0 – 10% centrality class for $\sqrt{s_{NN}} = 2.76$ TeV collision energy. In the case of charged jet observables, scaling factors were extracted from proton-proton collisions, both on the jet energy and also on spectrum normalization[34]. These factors allow us to compare the analysis of full jets and charged jets. We extract them by matching the spectra of a given observable in pp collisions by scaling it. It is then assumed that the factors are the same in heavy-ion collisions. An example is the jet p_T , in this case, since charged jets have fewer particles, its momentum will be smaller, and scaling for comparison is necessary. A factor of 3/2 was obtained in [34].

To include the new medium profile in JEWEL, a choice was made to build a grid with local values of the temperature. The spacing of the grid is about 0.15 fm. The time-step was taken to be 0.1 fm/c. The information was then passed to JEWEL upon request through a function $T(x, y, \tau)$. The τ coordinate is the proper-time and the x and y coordinates are the transverse coordinates, relative to the beam axis. τ was taken to be equal $\sqrt{t^2 - z^2}$ according to a boost invariance assumption. If one chooses not to make this assumption, a 3+1 code simulation for the hydrodynamics is necessary. The restriction to mid-rapidity of all analysis was then used. For values outside the gridpoints, a bicubic interpolation was used[35], and on the proper-time coordinate, a linear interpolation was used.

Since only a temperature profile was provided to JEWEL, a choice of an EOS had to be used to provide a density of scattering centers profile. This was used through an ideal equation of state. The density of scattering centers was taken as $n \propto T^3$. This is the dependence as one would have for the formalism described in Section 2.2. Also, no local fluid velocity was assumed. Any momentum that the scattering centers might have comes from a kinetical

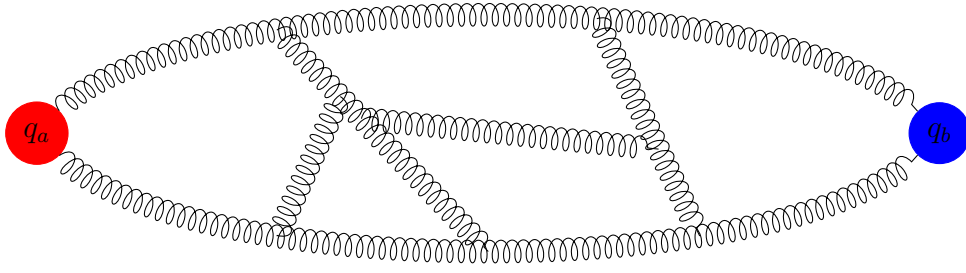


Figure 3.1: Schematics of force lines created by gluon trajectories between quarks.

description.

3.2 Jet Algorithms

Jets are a consequence of the confinement property of strong interactions[1, 4, 36]. It happens because the energy of partons coming out of a hard scattering grows linearly with their distance. This makes it energetically favorable for the system to convert this color dipole into a multi particle state of color neutral hadrons. One common picture of this is that the field between a parton dipole is seen as a tube connecting them. It is a consequence of the self-interaction of the gluon field that the lines of force do not spread out into space, but are contained in the space between the partons, this situation can be seen in Figure 3.1. Once the distance between the partons starts to grow, the energy stored in this flux-tube starts to grow linearly. Eventually, it becomes favorable for the system to exchange a portion of this tube for a pair of partons pulled out of the vacuum, turning it into two pairs of partons with two chromoelectric tubes. The process continues repeatedly until the energy in each pair is no longer enough to break the strings. At this point, these less energetic systems decay into the known hadron states.

Armed with the qualitative idea of what a jet is, a definition must be made in a more quantitative ground. This definition must account for certain conditions that are defined in the Snowmass accord[36]:

- Simple to implement in an experimental analysis;
- Simple to implement in the theoretical calculation;
- Defined at any order in perturbation theory;
- Yields finite cross sections at any order of perturbation theory;

- Yields a cross-section that is relatively insensitive to hadronization;

The difficulties that the previous accord tried to address are related to the fact that jets are ill-defined objects. There is a major uncertainty because jets are a consequence of non-perturbative physics, which is poorly understood. The way one defines a jet, then, is by defining an algorithm that clusters particles into jets. With this algorithm, experimental analysis can be performed. On the theory side, one usually implements a model for fragmentation and hadronization and later applies the jet algorithm to the final state to make comparisons with data. There is also the alternative to invoke parton-hadron duality and claim the jet 4-momenta are directly comparable to partons momenta[2].

Building an algorithm might have some difficulties due to infinities that appear in calculations at the theoretical level. Some of these infinities might be washed away from the calculations by grouping different final states together. The problem, then, is that the algorithm must treat these final states on the same ground as well.

One of these situations arises when a parton splits collinearly. This situation is illustrated in Figure 3.2. The loop diagram for the case that the partons merge again cancels its divergence with the case in which the partons split and do not merge. This means that, at the theoretical level, the two cases must be treated at the same level. In Figure, we see the difference between theoretically safe and an unsafe algorithm. An unsafe algorithm might see a hard seed on the high transverse momentum particle on the left and cluster from there. This would result in two jets. A safe algorithm would not be subject to this problem.

Another type of problem that might occur is due to soft radiation. This situation can be seen in Figure 3.3. As before, we have two final states that must be treated on the same ground, from the theoretical perspective. But the algorithm might not do so. It can happen because the extra particle seen in red in the Figure might act as a new seed and cluster two jets into one. Algorithms that succeed in avoiding this merging are called infrared safe.

One of the algorithms that satisfy to a good extent these criteria is the anti-kt algorithm[33]. The anti-kt algorithm belongs to a broader class called the recombination algorithms. The members of this class are all based on the idea of a distance defined between every pair of particles being analyzed. If the distance is smaller than the distance of another particle to the beam, the particles are combined. This process is repeated until no single pair satisfies the condition and one ends up with a set of jets of the event. At this stage, further cuts might be done in the rapidity or the p_t of the jet. The distance used in the anti-kt algorithm is defined by

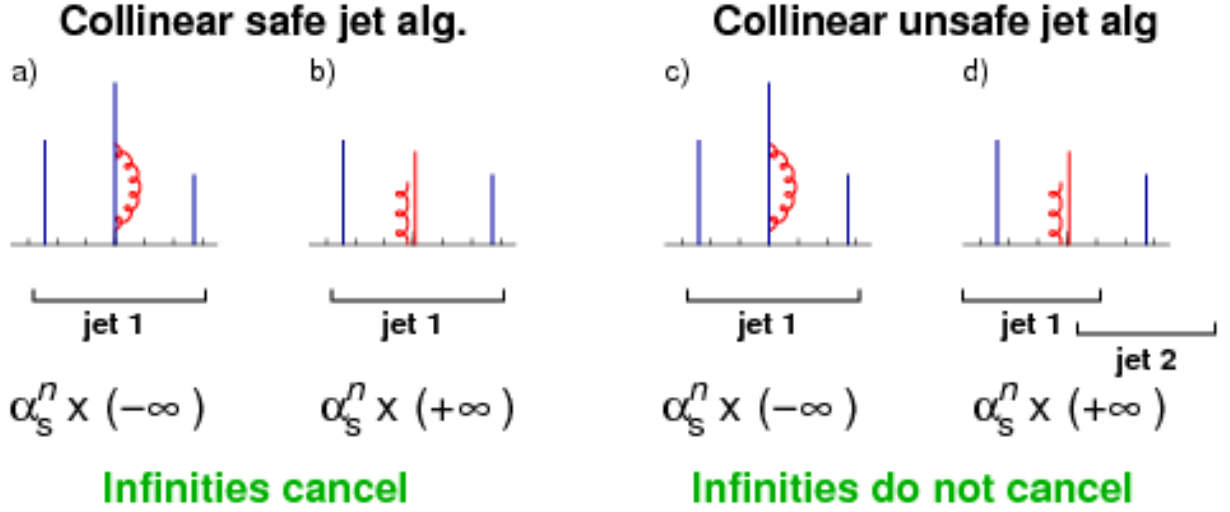


Figure 3.2: A description of collinear safe and an collinear unsafe algorithm. Here we have two situations that must be treated on equal grounds due to theoretical reasons and might not be so due to the choice of jet algorithm. Figure from [36]

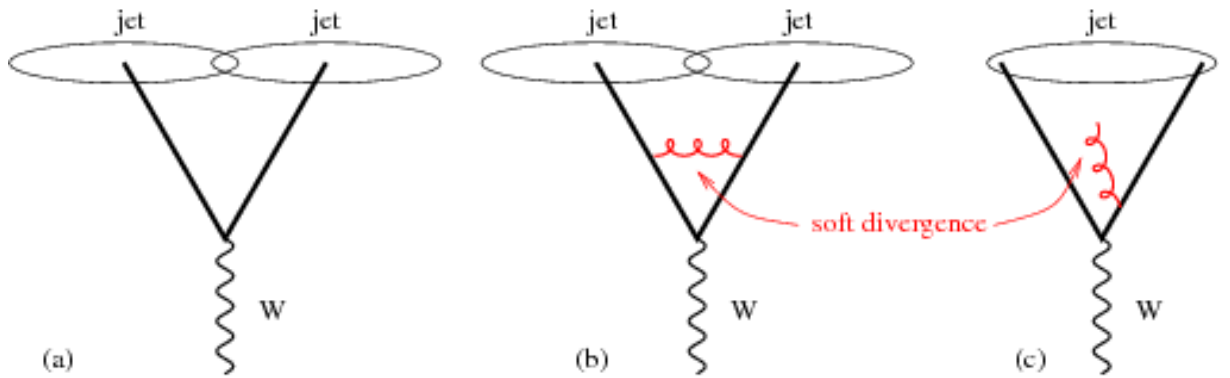


Figure 3.3: A description of infrared safe and an infrared unsafe algorithm. Here we have two situations that must be treated on equal grounds due to theoretical reasons and might not be so due to the choice of jet algorithm. Figure from [36]

the following equation:

$$d_{ij} = \min(p_{ti}^{2p}, p_{tj}^{2p}) \frac{\Delta R_{ij}}{R} \quad (3.1)$$

Where R is a parameter that is defined at each analysis. For $p = -1^4$. Where:

$$\Delta R_{ij} = \sqrt{(\eta_i - \eta_j)^2 + (\phi_i - \phi_j)^2} \quad (3.2)$$

A distance to the beam axis is also defined:

$$d_i = p_{ti}^{-2} \quad (3.3)$$

From all the d_{ij} and d_i the minimum value is chosen. If it is d_i then this particle is removed from the list and called a jet. Otherwise, it is a distance d_{ij} , the i and j particles are combined. The process goes on iteratively until a final list of jet candidates is left. The recombination of the particles is performed using the E scheme, or 4-momentum scheme, which means particles are combined by adding their 4-momenta. This process is illustrated in the Figure 3.4.

3.2.1 Background subtraction

An extra difficulty arises when trying to perform jet analysis in heavy-ion collisions due to the background contamination, called the Underlying Event (UE). The UE corresponds to the soft particles that come from the radiation of the freeze-out surface and are mainly explained through hydrodynamics. When one is trying to cluster jets, experimentally, one must subtract this background in order to make comparisons with theory.

In JEWEL, the recoiling scattering centers can be kept and included in the final state of the events. Whenever there is an elastic collision during the parton propagation, the distinction between the 4 momentum that is part of the jet and the 4 momentum that is part of the medium is spoiled. To address this problem, the scattering centers kept by JEWEL are used to subtract this 4 momenta from the final state.

Following [34], the background subtraction is performed by the use of ghost particles. These particles are inserted into the final state with very low p_T and the same direction as the four-momentum assigned to the scattering center. Particles are then classified as background if

⁴The value $p = 1$ corresponds to the k_t algorithm and $p = 0$ to the Cambridge-Aachen. See [36] for further details

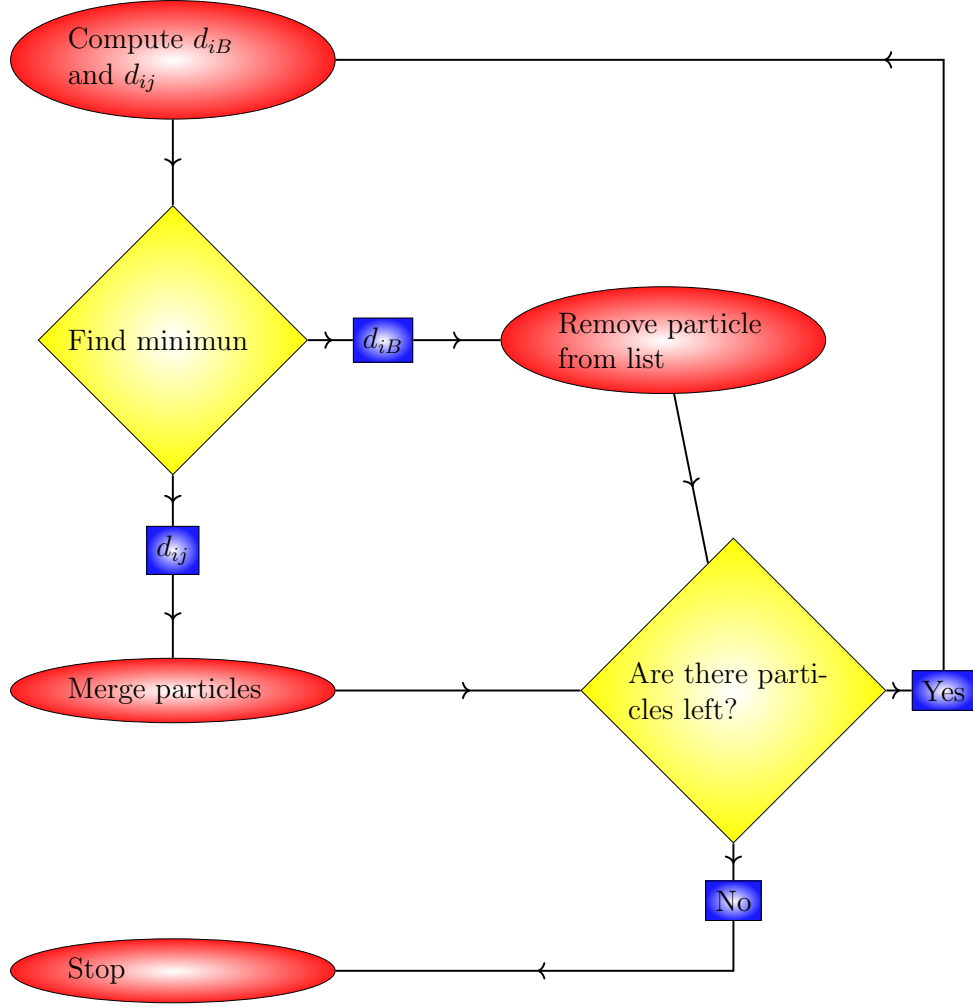


Figure 3.4: Flow diagram for the anti-kt algorithm.

they satisfy the following condition:

$$\Delta R_{ij} < 1 \cdot 10^{-5} \quad (3.4)$$

Where ΔR_{ij} is the distance to the closest ghost particle (see Equation (3.2)). The list compiled by evaluating this condition is then subtracted according to each observable. In the case of jet girth, for instance, the particles deemed to be background are removed from the jet constituents list and thus do not participate of the observable calculation. In the case of jet dispersion, we used:

$$p_T^D = \frac{\sqrt{\sum_{\text{particles}} p_t^2 - \sum_{\text{background}} p_t^2}}{p_{t,\text{corrected}}^{\text{jet}}} \quad (3.5)$$

For the jet mass, a correction of the jet four-momentum comes automatically when removing the background from the list of particles.

3.3 Jet Observables

Although the main idea of a jet is to reconstruct the basic partonic kinematics of a hard scattering, there are a lot of things that can be investigated with a jet. This is since the jet has more information than a single particle. One can study its shape and structure to find radiation patterns and non-perturbative dynamics. In the present work, the main idea is to look for radiation patterns. Here we define the observables that can characterize the jets used in this work.

3.3.1 Girth

The generalized angularities for the jet constituents are defined as:

$$\lambda_{\beta}^{\kappa} = \sum_i \left(\frac{p_{T,i}}{p_{T,jet}} \right)^{\kappa} \left(\frac{\Delta R_{jet,i}}{R} \right)^{\beta} \quad (3.6)$$

Where κ , β and R are parameters chosen at each analysis. $\Delta R_{jet,i}$ is the angular distance between jet and constituent i . Girth is related to the angular opening of the jet. The idea is to pick the first order moment in angular distribution with the constituents p_T as weights. This means picking $\beta = \kappa = 1$. Girth is defined by:

$$g = \sum_{\text{constituents}} \frac{p_t}{p_t^{jet}} \Delta R_{i,jet} \quad (3.7)$$

Where $\Delta R_{i,jet}$ is calculated according to (3.2) and the sum is taken on the constituents of the jet. Its possible values lie in the $[0, 1]$ interval. Girth is also known in some collaborations as jet width. Unlike the jet mass, it depends linearly on the transverse momentum of the constituent particles. Therefore, it is more sensitive to softer fragmentation.

3.3.2 Dispersion

This observable measures the *hardness* of the fragmentation of the jet. This means that it will have a large value if the jet p_t is distributed in fewer particles, and smaller values if the p_t is distributed in a larger number of particles. Its definition is given by the equation:

$$p_T^D = \frac{\sqrt{\sum_{\text{constituents}} p_{t,i}^2}}{p_t^{jet}} \quad (3.8)$$

Where the sum is taken on the constituents of the jet. It corresponds to $\kappa = 2$ and $\beta = 0$ in Equation (3.6). It can be seen from its definition that the possible values lie in the $[0, 1]$ interval. Values close to one will correspond to the extreme case of the jet transverse momentum being distributed in one or two constituents and one of them carries most of its momentum. The opposite limit corresponds to the jet transverse momentum being distributed almost equally on a high number of constituents.

3.3.3 Jet Mass

The jet mass is a observable that is constructed from the jet four-momentum in the usual Lorentz formalism. The definition is:

$$M_J = \sqrt{\left(\sum_{\text{particles}} E\right)^2 - \left(\sum_{\text{particles}} \vec{p}\right)^2} \quad (3.9)$$

It can be seen, in the RHS of the above equation that this observable is sensitive to the collimation of the jet. This can be observed by noting that, inside the square root, there is a scalar sum and a vector sum, where vector sum depends on the angular separation of the constituents. The broader the jet, the smaller the jet mass. And the impact of each constituent particle in this observable depends on the squared transverse momentum. This increases the impact of the harder constituents of the jet.

3.3.4 Azimuthal anisotropy v_2

The azimuthal anisotropy for a given observable comes from the idea of expanding a given spectrum in the following form:

$$\frac{dN}{d^2p_T d\eta d\phi} = \frac{dN}{d^2p_T d\eta} \left[1 + \sum_n 2v_n \cos(n(\phi - \Psi_{\text{RP}})) \right] \quad (3.10)$$

Where Ψ_{RP} is the reaction plane angle. The coefficients v_n are adjusted and represent the lack of cylindrical symmetry of the spectra. v_2 is called the azimuthal anisotropy coefficient and v_3 is the triangular flow. They usually reflect the geometry of the initial conditions set by the early dynamics, before the hydro phase. The harder problem in the measurement of these quantities is the determination of the reaction plane, which is random. Usually, it is calculated by adjusting the above formula with the distribution in ϕ of the observed particles in an event.

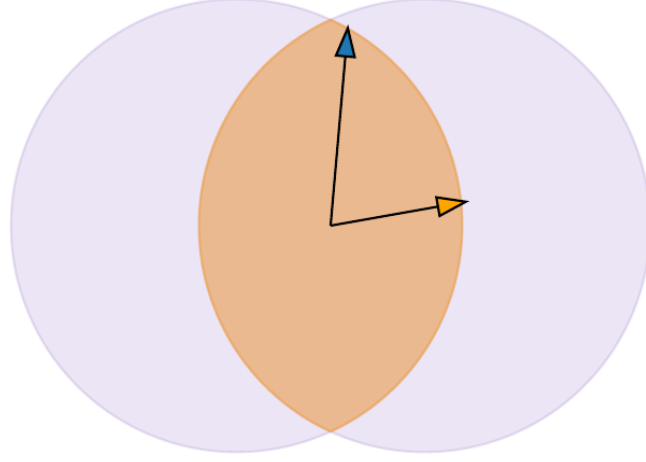


Figure 3.5: Schematics of path length dependence of jet quenching. The blue arrow represents a longer trajectory for a parton, and therefore has a higher chance of losing more energy than the orange arrow.

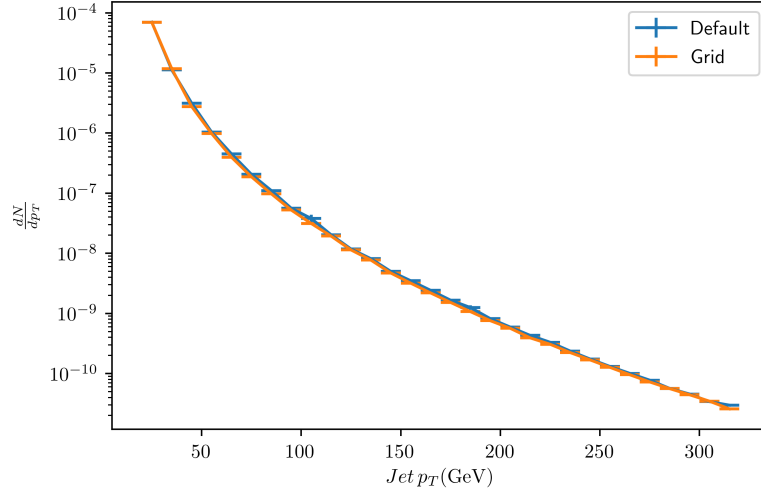
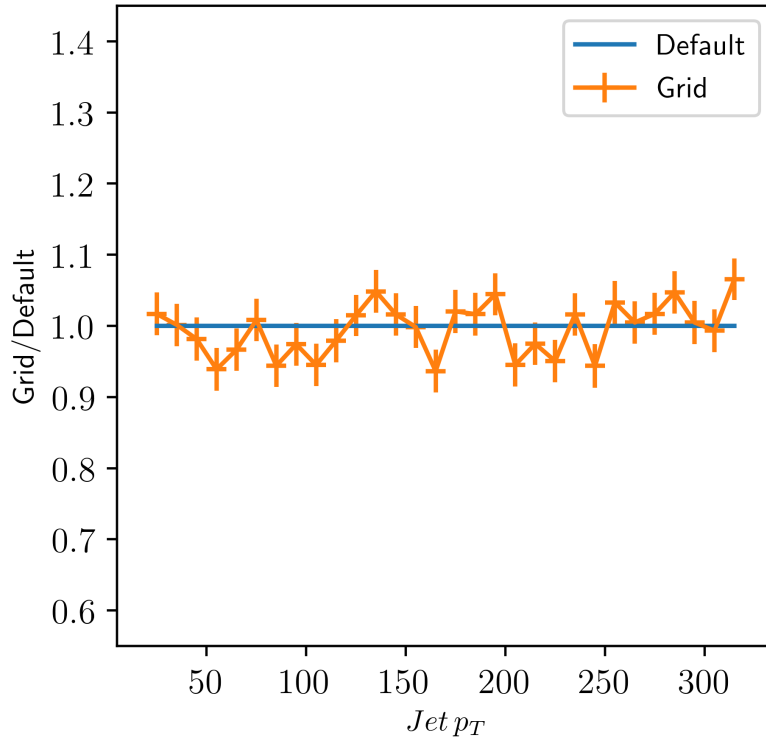
The v_2 coefficient is related to the ellipticity of the initial conditions for the hydro expansion. As can be seen in Figure 4.19, it comes from the shape of the overlap zone of the colliding nuclei.

3.4 Grid validation

As a validation for the grid method implemented in this work, we show here a comparison between observables calculated with JEWEL in its default configuration and with the grid method implemented here. In Figure 3.6 we can see the jet p_T spectrum for both cases. And in Figure 3.7 we can see a ratio plot of both spectra. Within the statistical uncertainty calculated for the Monte Carlo, we can see that they both agree. This result shows that errors inserted due to interpolation of the grid do not affect this observable.

For the case jet mass we can see a plot of the spectra and a ratio plot on Figures 3.8 and 3.9, respectively. The mass has an error of 25% in only one bin, but the rest of the bins is well controlled within the uncertainties. This shows that both methods agree. The peak and width of the distribution are well reproduced.

On Figures 3.10 and 3.11 we can see the plots for the jet girth for both cases and also a ratio plot. The qualitative behavior is reproduced. Within the uncertainties, the data of both methods

Figure 3.6: Jet p_T for Grid validation.Figure 3.7: Grid/Default for jet p_T

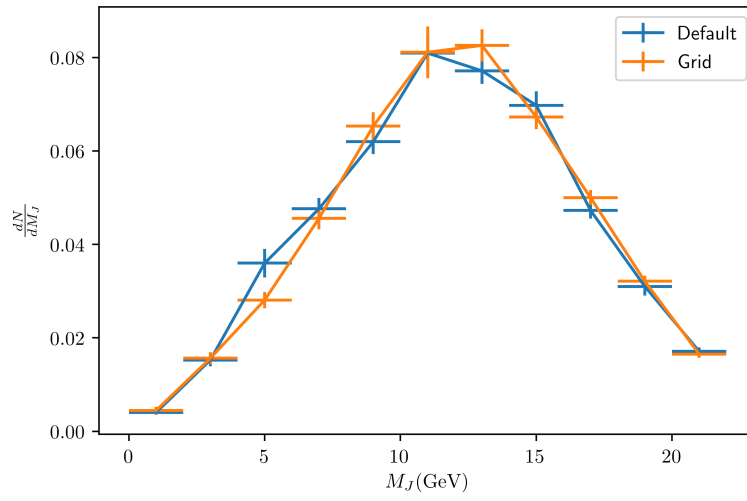


Figure 3.8: Jet Mass for Grid validation.

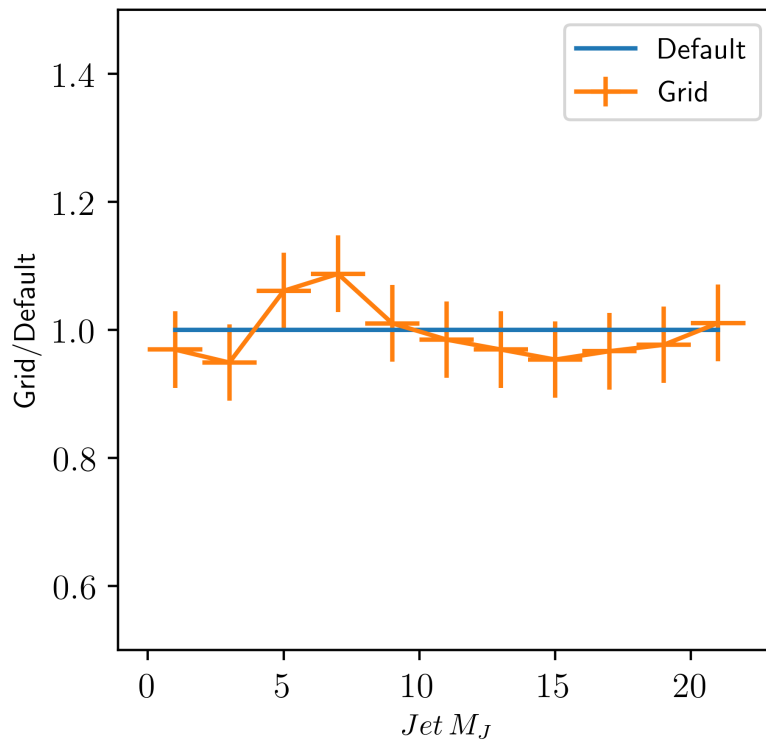


Figure 3.9: Grid/Default for jet mass

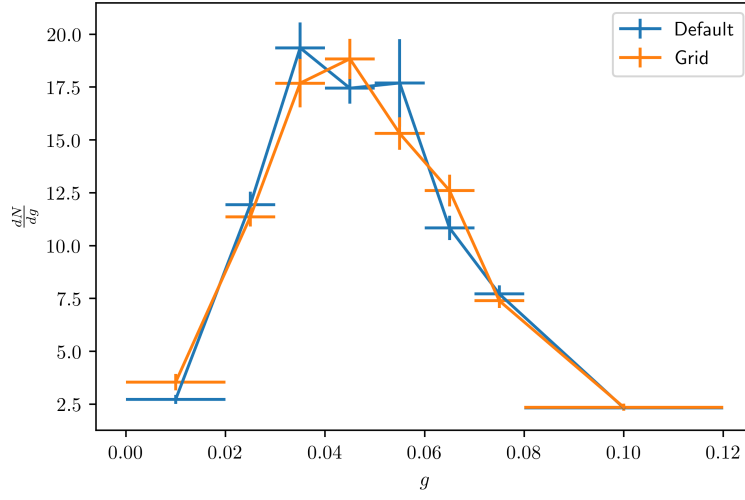


Figure 3.10: Jet Girth for Grid validation.

agree. The peak and width of the distribution are well reproduced.

On Figures 3.12 and 3.11 we can see the plots for the jet p_T^D for both cases and also a ratio plot. The qualitative behavior is reproduced. Within the uncertainties, the data of both methods agree. The peak and width of the distribution are well reproduced.

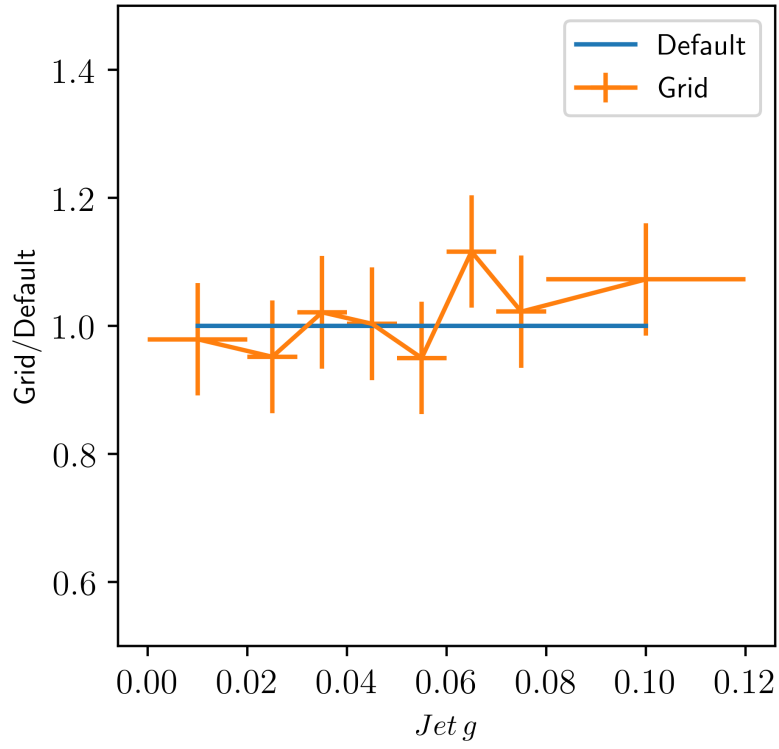


Figure 3.11: Grid/Default for jet girth

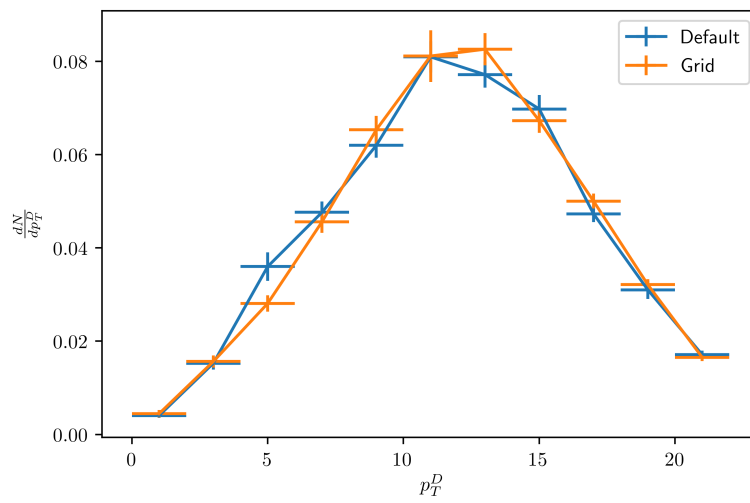


Figure 3.12: Jet Dispersion for Grid validation.

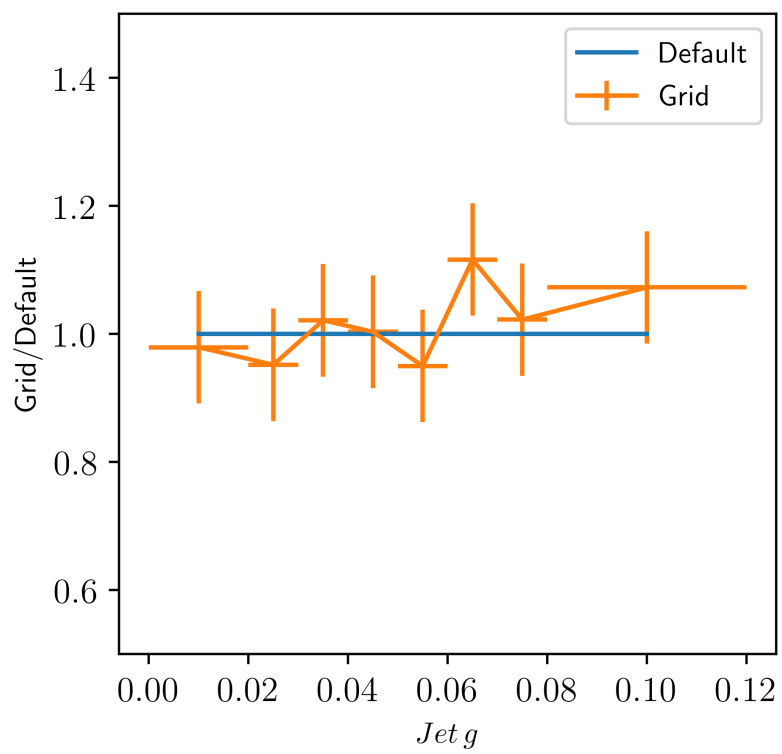


Figure 3.13: Grid/Default for jet dispersion

Chapter 4

Results

4.1 Experimental Results

Before showing the results of the simulations, it is interesting to discuss the experimental results for the studied observables. They indicate that jets suffer modifications due to interactions with the dense and hot medium created in relativistic heavy-ion collisions. The first of these, and most inclusive one is the jet p_T . We can observe in Figure 4.1 that the PbPb spectrum is suppressed when compared to the pp spectrum. The same trend is observed when central and semi-peripheral collisions are compared: the former is more suppressed than the later. This indicates that there is suppression of jets for PbPb collisions, and that this suppression is also related to centrality. The fact that it varies with the centrality is also an evidence that this suppression has its origin in the interaction with the medium. Higher centrality implies higher energy densities, which in turn implies higher chance of forming the Quark-Gluon Plasma,. In the Figure 4.2 we see that the PbPb spectrum can be 20% that of pp for lower transverse momentum, and saturates at no more than 60% for higher values of p_T .

There is also evidences that this suppression is path length dependent. This can be seen in Figure 4.3 where several measurements of v_2 are presented. The data in orange and in white circles are measurements of the v_2 . They come from ALICE and CMS collaborations respectively. The fact that it grows linearly for lower p_t is predicted by modeling collective behavior. For $p_T \gtrsim 5$ GeV, the particles are not usually thermalized. The description of the particles as Jet Quenching then comes into play. We see in the plot that the v_2 continues to be non-zero well above 5 GeV. This indicates that the energy loss of this partons must be path length dependent. The fact that it depends also on centrality is evidence that this comes from the interaction of

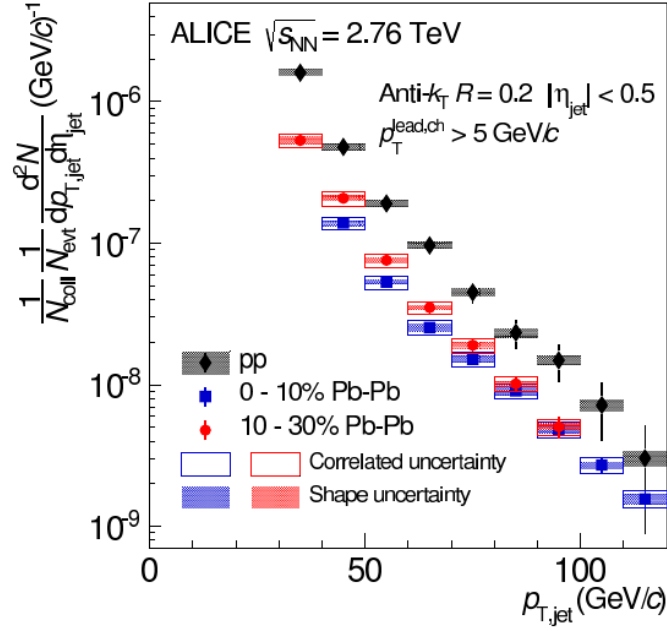


Figure 4.1: The spectra of $R = 0.2$ jets with a leading track requirement of $5 \text{ GeV}/c$ in $0 - 10\%$ and $10 - 30\%$ most central PbPb collisions scaled by $1/N_{coll}$ and in inelastic pp collisions at $\sqrt{s_{NN}} = 2.76 \text{ TeV}$. Plot from [37]

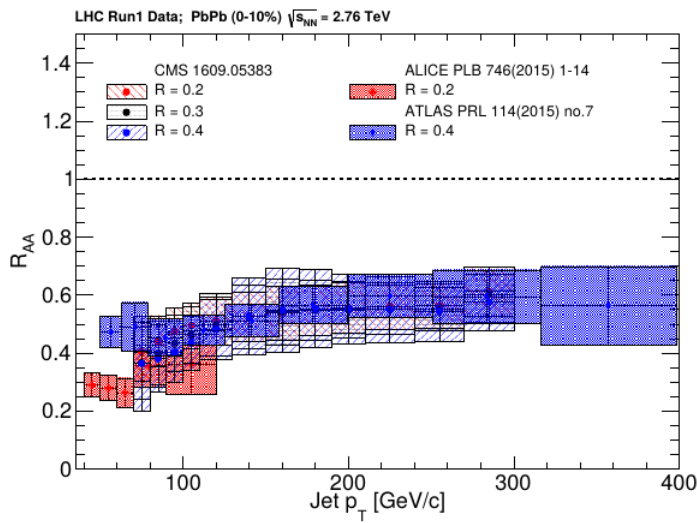


Figure 4.2: Jet p_T R_{AA} measured in different collaborations. Figure from [38].

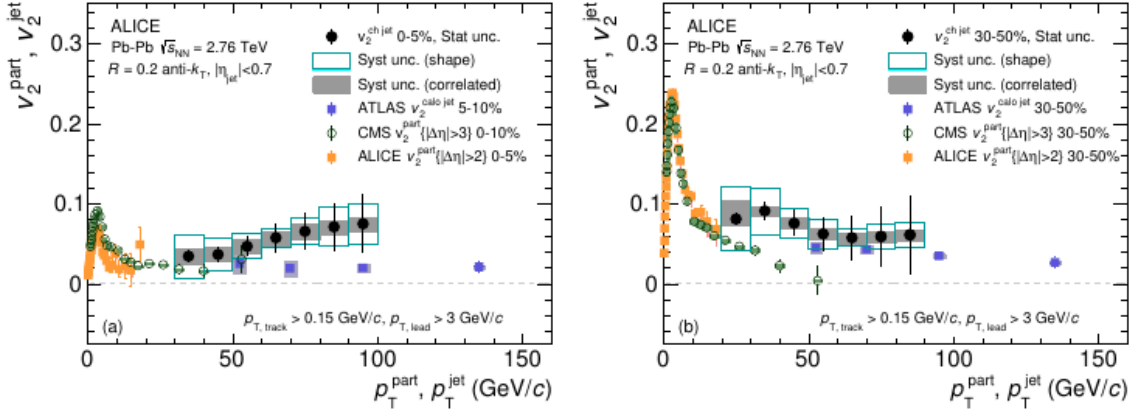


Figure 4.3: Jet v_2 measured in different collaborations. Figure from [38].

high energy partons with the medium. The data in black circles comes from ALICE collaboration, and in blue squares come from ATLAS collaboration. This data is different from the previous cases since it uses reconstructed jets. ALICE reconstructs jets with the TPC, so only charged particles are included in the analysis. ATLAS uses the hadronic calorimeters, which means it measures full jets. Measuring only charged particles implies, for the same jet, measuring less particles, which imply less p_T for the same jets. This explains the difference in scale of the reconstructed jets observed in Figure 4.3. For semi-central and central collisions, the collaborations do not agree upon a re-scaling of jet momenta. ALICE measures a higher value for v_2 .

In Figure 4.4 we see measurements of the girth and p_t^D for charged jets with small radius ($R = 0.2$) jets. The simulations for pp describe well the data for these observables[39], this can be seen on Figure 4.5. There is a modification if compared with the simulation also displayed in the plot. The girth indicates more collimated jets. The p_t^D indicates harder fragmentation if compared to the pp case.

Regarding jet mass, the first measurements can be seen in the Figure 4.6. In the Figure, the mass measured in PbPb collisions is compared to pPb collisions. pp data for jet mass is well described by simulations. In [40] the comparison of pPb with simulations for pp show that there are no cold matter nuclear effects on this observable. So the comparison of PbPb with pPb would show only the effects of the hot QGP on the partons. For jets on the range 60 – 100 GeV range, the jets in PbPb tend to have slightly lower mass than those of pPb. This indicates a broadening of the jet.

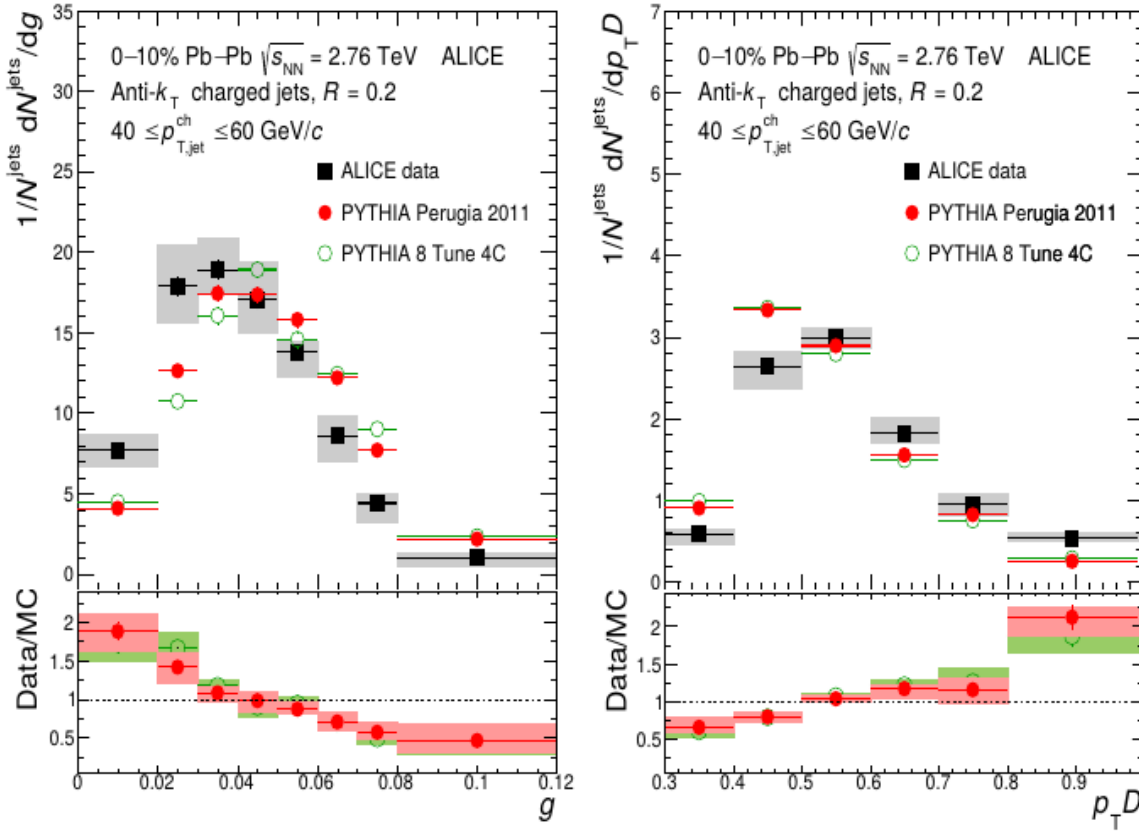


Figure 4.4: Girth and p_t^D measured by ALICE collaboration. Figure from [39].

4.2 JEWEL results

JEWEL was developed to describe data from heavy-ion collisions. And it can reproduce most inclusive data. An example is displayed in Figure 4.7. In the Figure we can see the prediction for neutral pion p_t spectrum suppression, as measured by PHENIX collaboration. It was one of the first results to indicate the phenomenon of Jet Quenching. In Figure 4.8 we can see the suppression for charged hadrons compared to data from ALICE and CMS collaborations. JEWEL describes this inclusive data really well. Also, in Figure 4.9 we can see that the suppression for reconstructed jets is also well described by JEWEL. The two Figures combined show that JEWEL can handle a wide energy range and different hadrochemistry well.

Studying internal jet structure, we can see a somewhat different picture of JEWEL performance. For instance, in Figure 4.10 we see that JEWEL predicts jets broader than data. The jet mass can be seen in Figure 4.11. We are interested in this work in the case with the recoiling scattering centers, since radiation patterns trying to probe the medium is our goal. JEWEL also predicts higher values for this observable, indicating broader jets than expected. In the case without recoils, the jet mass has lower values than data, which indicates a hardening of the core.

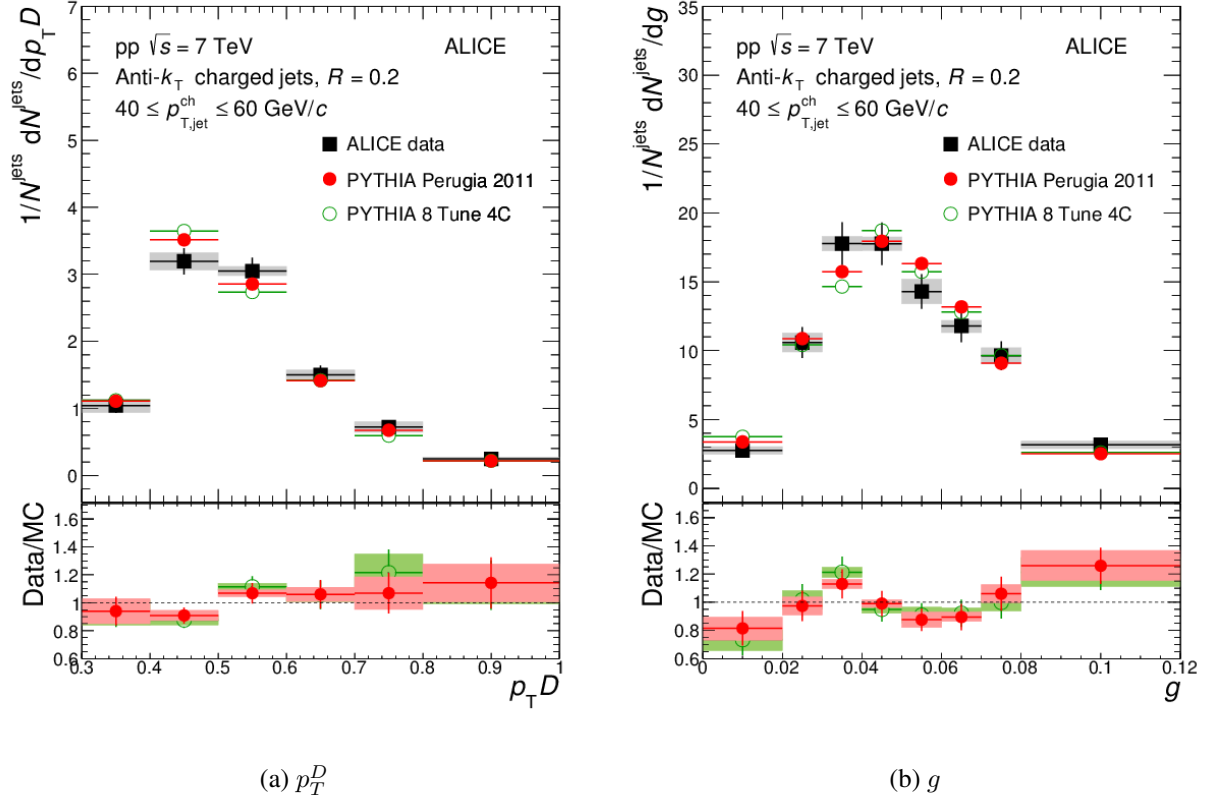


Figure 4.5: Measurements of both p_T^D and g compared with simulations for pp collisions. Figure from [39].

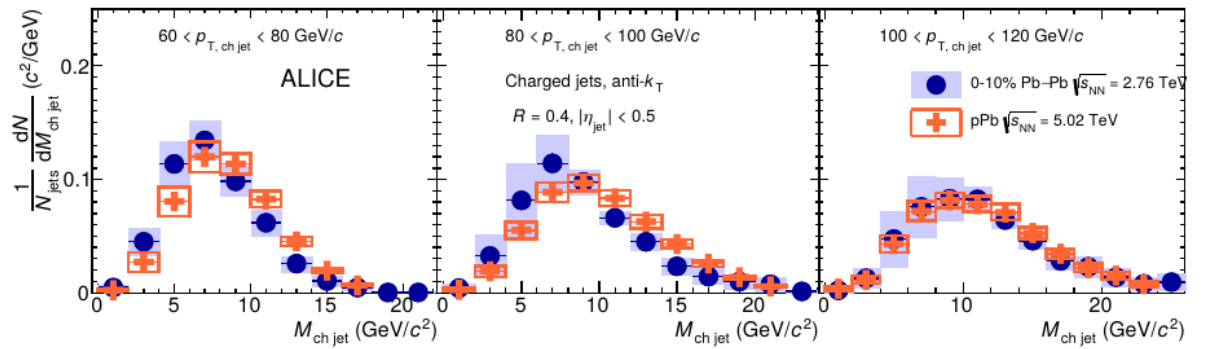


Figure 4.6: Jet mass measured by ALICE collaboration. Figure from [40].

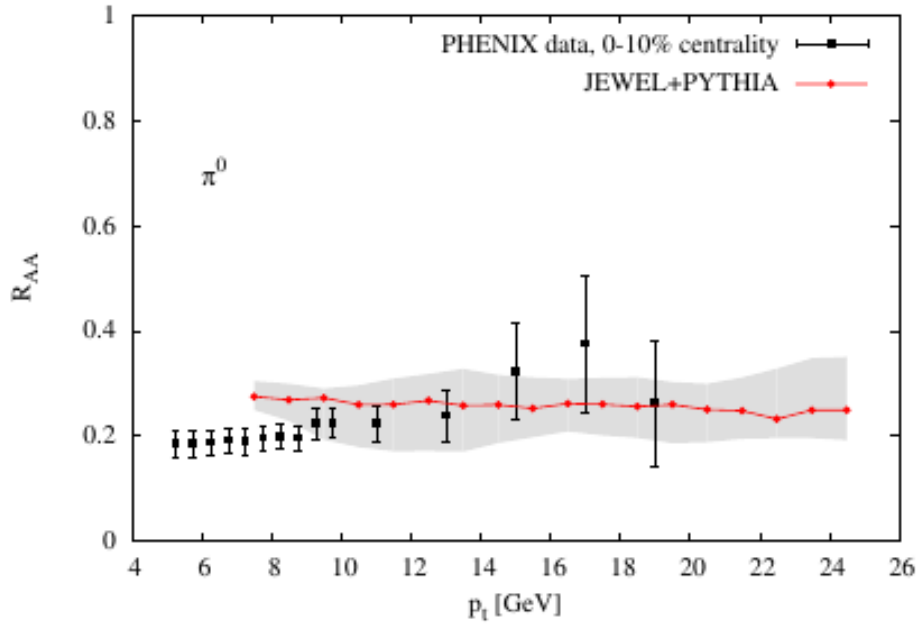


Figure 4.7: Hadron R_{AA} as measured by the PHENIX collaboration compared to JEWEL predictions. Figure from [23].

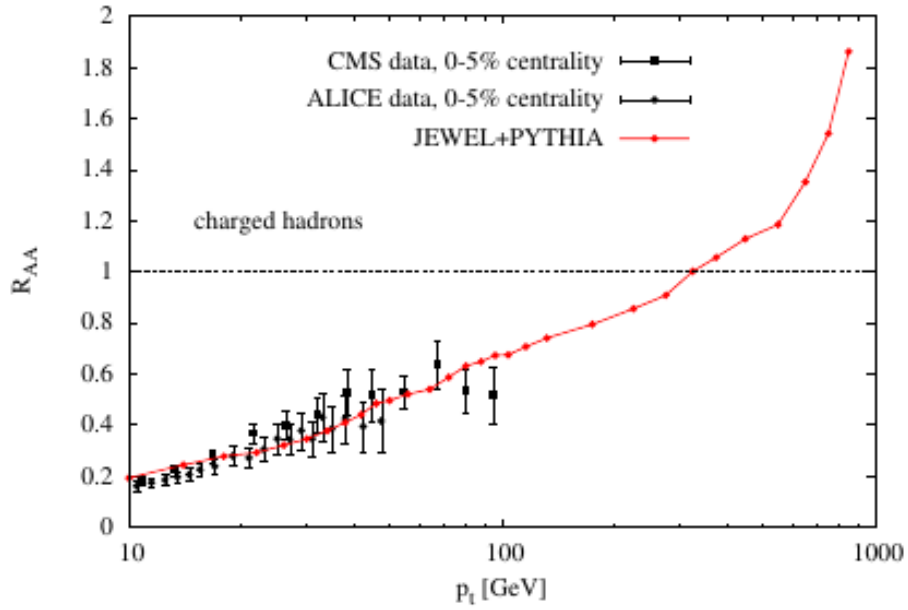


Figure 4.8: Hadron R_{AA} as measured by CMS and ALICE collaborations compared to JEWEL predictions. Figure from [23].

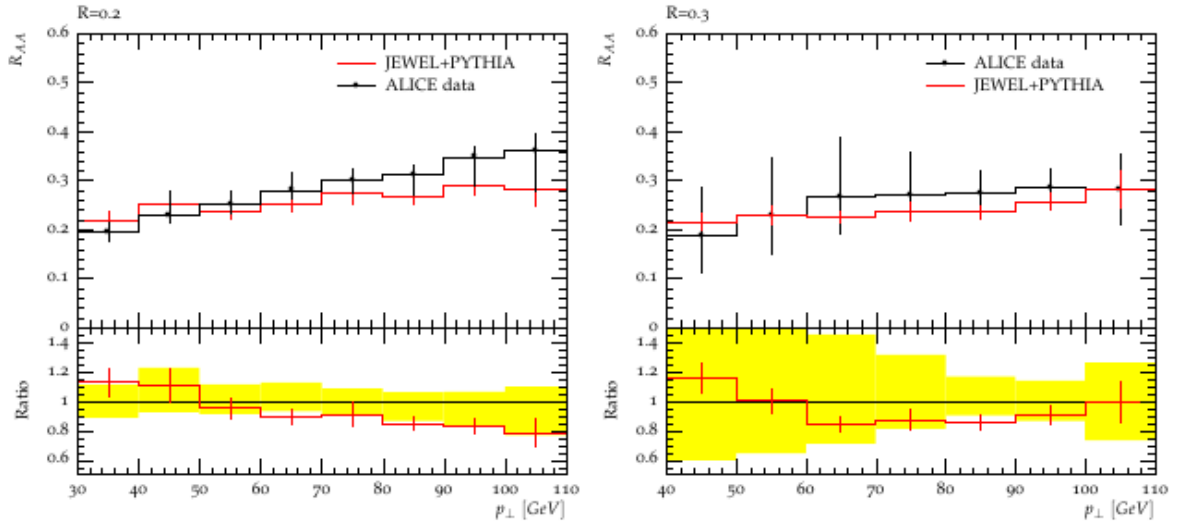


Figure 4.9: Jet p_T R_{AA} as measured by CMS, ALICE and ATLAS collaborations compared to JEWEL predictions. Figure from [23].

4.3 JEWEL with realistic IC

In Figure 4.12 we see the results for jet girth with realistic initial conditions. Here T_{RENTTo} was used with calibration to fit IP-Glasma results[20]. JEWEL tends to overestimate the peak value even with the new initial conditions. One is reminded that girth is related to the angular opening of the jet. Girth also depends linearly on the transverse momenta of the particles. The overestimation of JEWEL results tells us that the jets produced by the simulation tend to be slightly broader than the jets from data. No further improvement comes from the inclusion of more realistic initial conditions, as the results given by the inclusion of realistic initial conditions agree with the default of JEWEL.

In Figure 4.13 we see the results for the jet dispersion. The default of JEWEL predicts slightly lower values than data. This indicates softer fragmentation. With the inclusion of realistic initial conditions, there is no substantial difference.

The results for the jet mass are displayed in Figure 4.14. Here we present also the inclusion of realistic IC for this observable. JEWEL in its default does not make a good prediction for it already. The problem is of the same nature of the disagreement of the girth, but worst. The jets in data tend to have a lower mass than predicted, this indicates larger jets, as is the case with girth. The mass further indicates that the problem lies in the soft fragmentation, which depends strongly on hadronization. There is some improvement from the addition of the realistic IC background, as one can see from the slight shift to the left. This shift is not significant though,

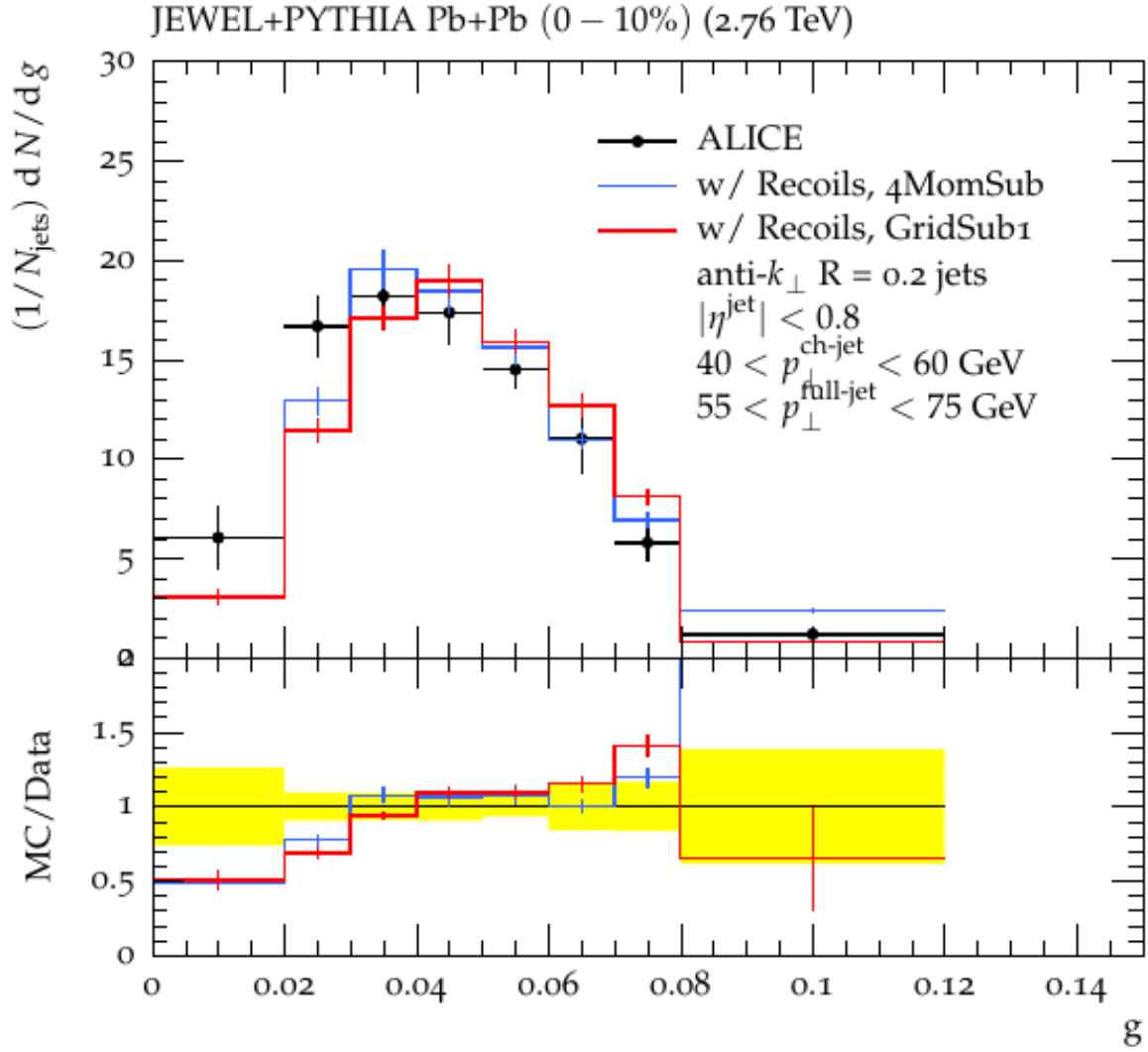


Figure 4.10: JEWEL predictions for jet girth compared to measurements from ALICE collaboration. Figure from [41].

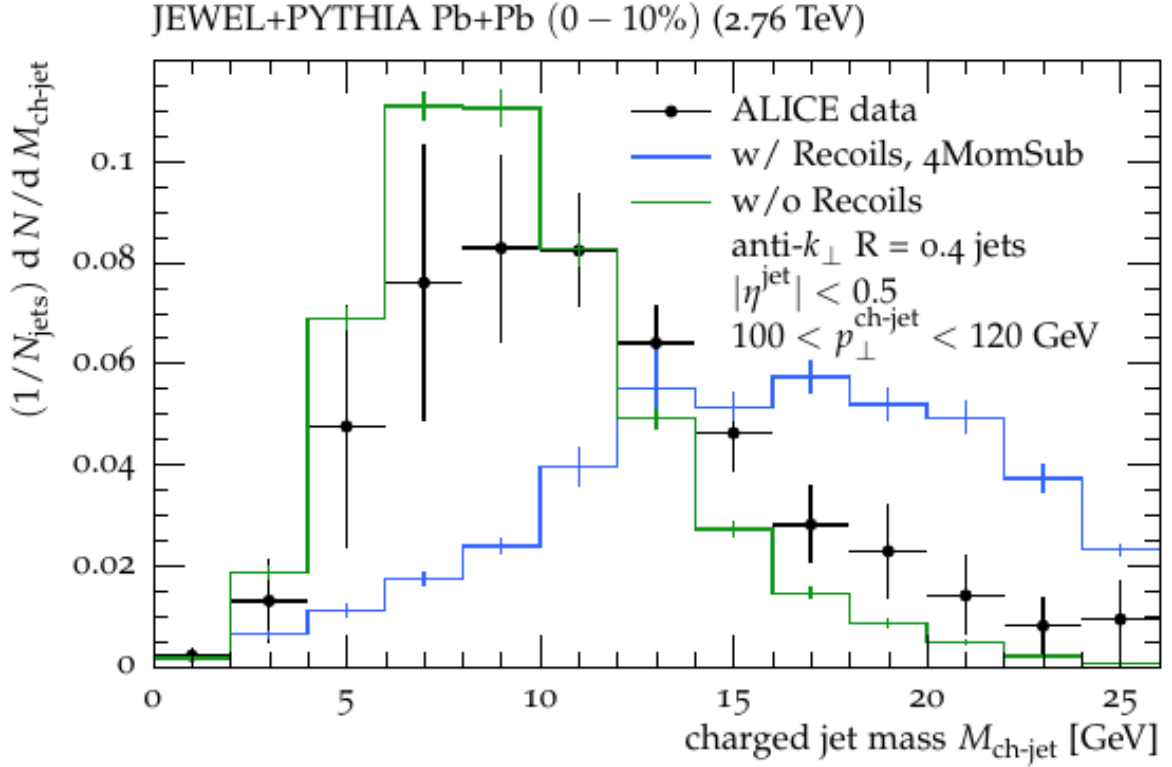


Figure 4.11: JEWEL predictions for jet mass compared to measurements from ALICE collaboration. Figure from [41].

due to the uncertainties of the method. There is a discrepancy in the spectrum.

In Figure 4.15 we see the results for the jet v_2 . The data from ALICE and ATLAS show that there is tension between the experimental results making any conclusion about the performance of the model more difficult. ALICE uses their TPCs for jet reconstruction and ATLAS uses the hadronic calorimeters. This means that ALICE uses only charged particles, and ATLAS uses all hadrons for jet reconstruction. This explains why ALICE data has lower values of p_T . Although there is a disagreement between the collaborations, both data seems to indicate that the v_2 is different from zero. This is expected from fluctuations that happen on the initial conditions, since central collisions don't have a geometry that naturally raises an azimuthal asymmetry on the energy distribution. We can see in the Figure 4.15 that JEWEL, even with realistic IC, predicts values consistent with zero v_2 .

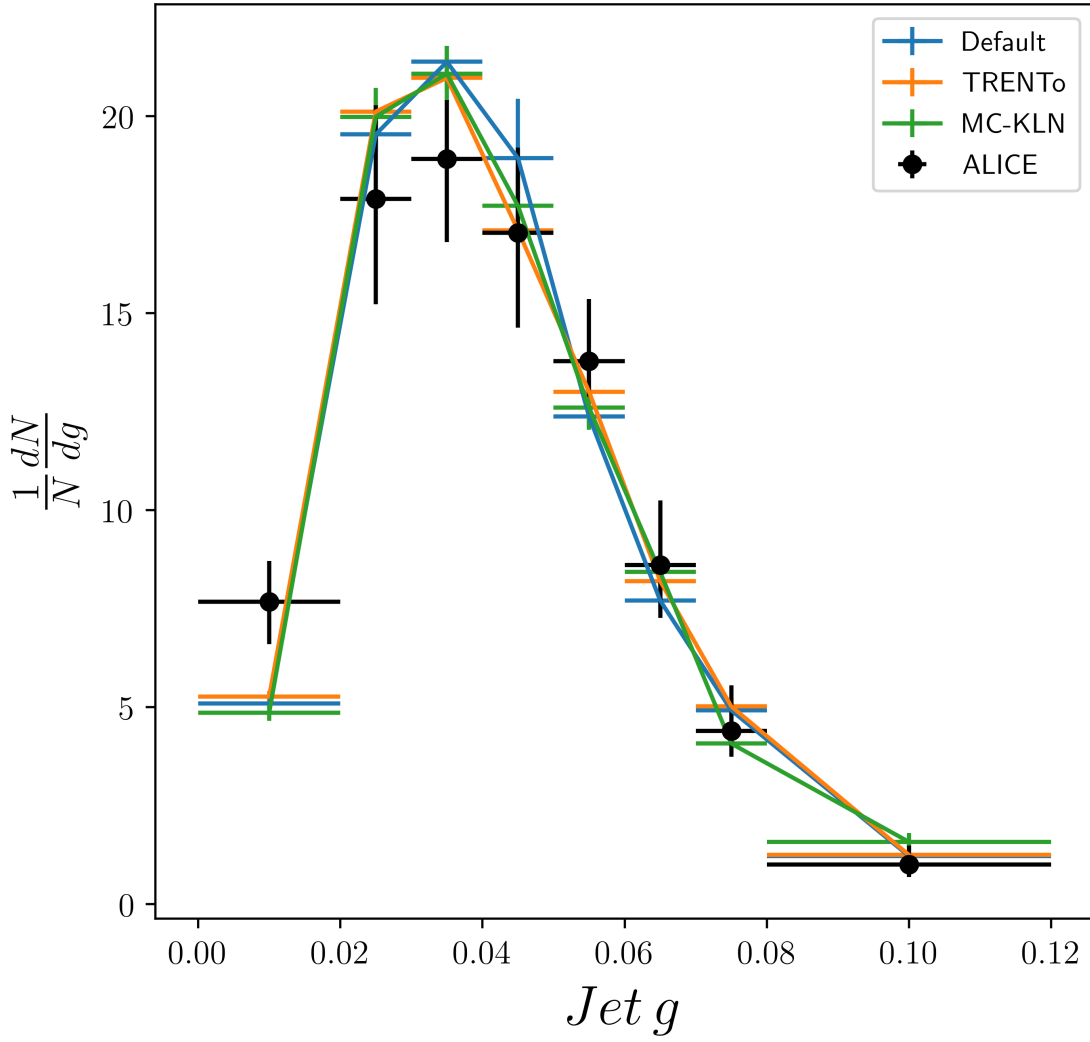


Figure 4.12: Jet Girth for charged jets calculated for $R = 0.2$ anti-kt algorithm and $|\eta| < 0.8$. $40\text{GeV}/c < p_T < 60\text{GeV}$. The CM energy is $\sqrt{s_{NN}} = 2.76\text{TeV}$. On the 0 – 10% centrality class.

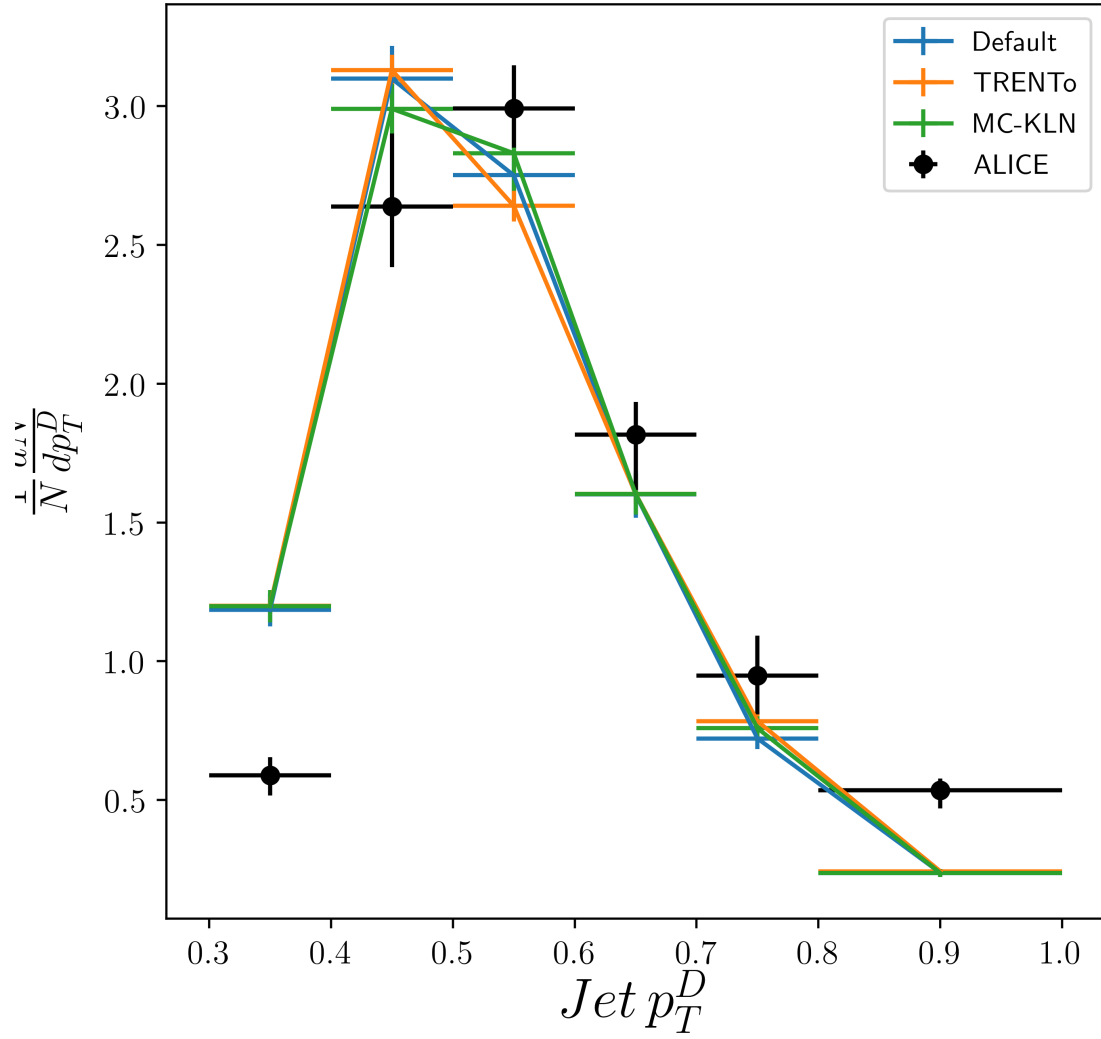


Figure 4.13: Jet Dispersion for charged jets calculated for $R = 0.2$ anti-kt algorithm and $|\eta| < 0.8$. $40\text{GeV}/c < p_T < 60\text{GeV}$. The CM energy is $\sqrt{s_{NN}} = 2.76\text{TeV}$. On the 0 – 10% centrality class.

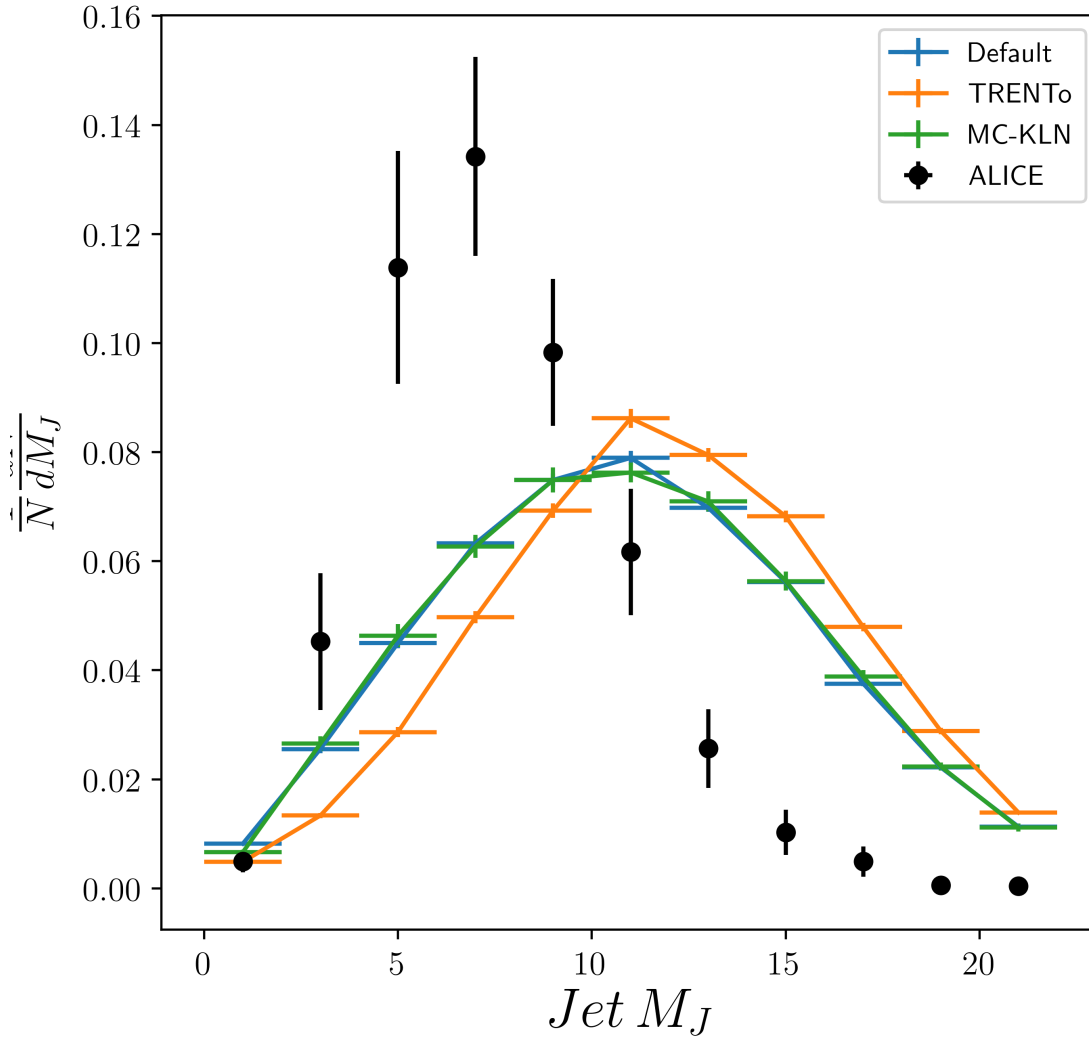


Figure 4.14: Jet Mass for charged jets calculated for $R = 0.2$ anti-kt algorithm and $|\eta| < 0.8$. $40\text{GeV}/c < p_T < 60\text{GeV}$. The CM energy is $\sqrt{s_{NN}} = 2.76\text{TeV}$. On the 0 – 10% centrality class.

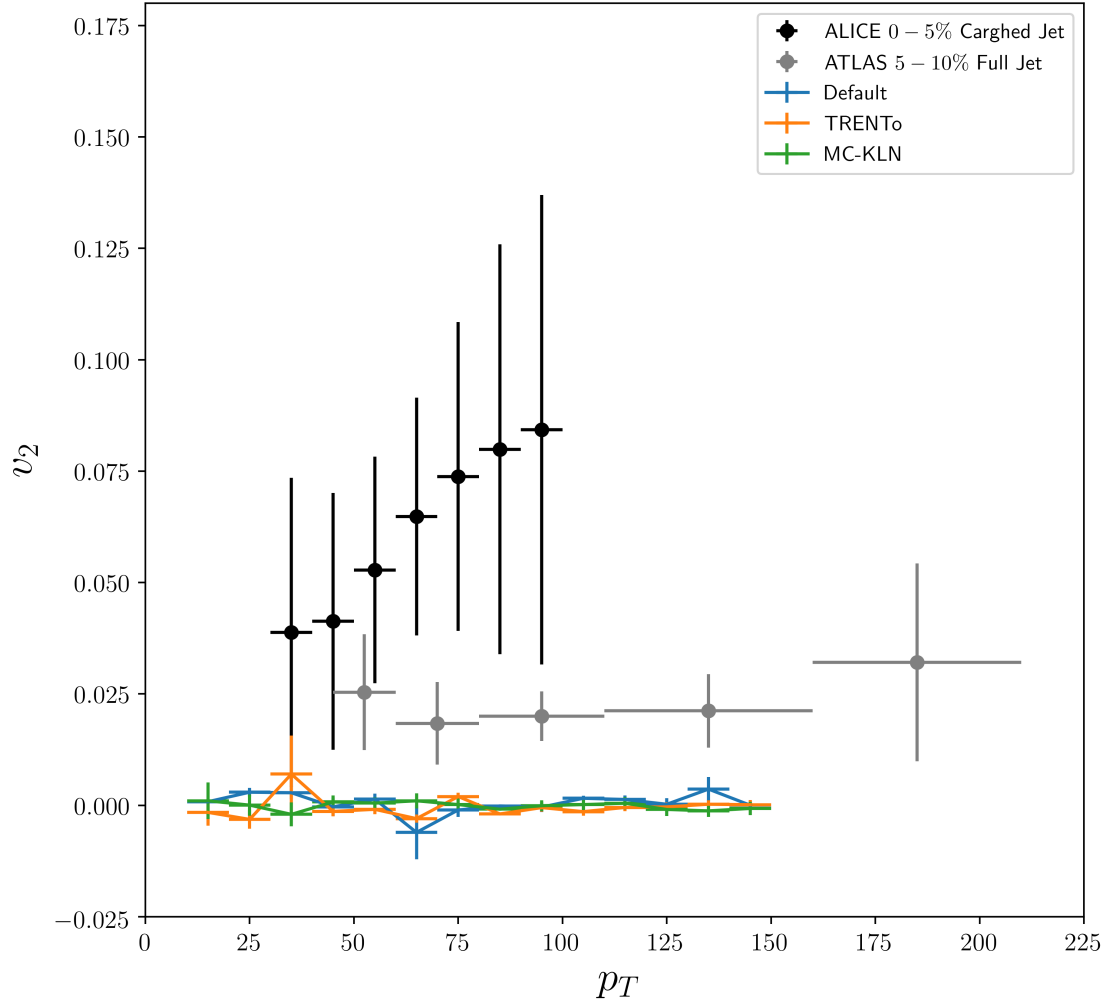


Figure 4.15: Jet v_2 calculated for $R = 0.4$ anti-kt algorithm and $|\eta| < 0.8$. The CM energy is $\sqrt{s_{NN}} = 2.76\text{TeV}$. On the 0 – 10% centrality class.

4.4 JEWEL with realistic hydro

In Figure 4.16 we see the results for jet girth. Considering the hydrodynamic expansion for the medium as well. The result shows that JEWEL tends to overestimate it. Since girth is related to the jet width, this shows broader jets than the data. No further improvement comes from the inclusion of more realistic initial conditions or hydrodynamics, as the results given by the inclusion of the realistic hydro and initial conditions agree with the default of JEWEL.

In Figure 4.17 we see the results for the jet dispersion with the inclusion of realistic hydro. The default of JEWEL predicts slightly lower values than data. This indicates softer fragmentation. With the inclusion of realistic hydro, the agreement is slightly worst for lower values, but not substantially different. This indicates that the fragmentation is slightly softer than that of the default. Regions of greater density on the profile could be responsible for the further soft radiation causing this.

The results for the jet mass are displayed in Figure 4.18. JEWEL in its default doesn't make a good prediction for it. The problem is of the same nature of the disagreement of the girth, but worst. The jets in data tend to have a lower mass than predicted, this indicates larger jets, as is the case with girth. The mass further indicates that the problem lies in the soft fragmentation, which depends strongly on hadronization. There is some improvement from the addition of the realistic hydrodynamics background, although there is a discrepancy in the spectrum.

In Figure 4.19 we see the results for the jet v_2 , with the inclusion of realistic hydro. Although there is a disagreement between the collaborations, both data seems to indicate that the v_2 is different from zero. The fluctuations might be responsible for the existence of the asymmetry. We can see in Figure 4.19 that the inclusion of the realistic hydro has raised the v_2 from zero, although there seems to be overestimating it. The simulations currently performed tell us that the combined effect of realistic initial conditions and hydrodynamics are responsible for this effect. The fact that neither MC-KLN nor T_RENTo have shown significant v_2 indicates that the hydrodynamics is an essential ingredient for describing this observable.

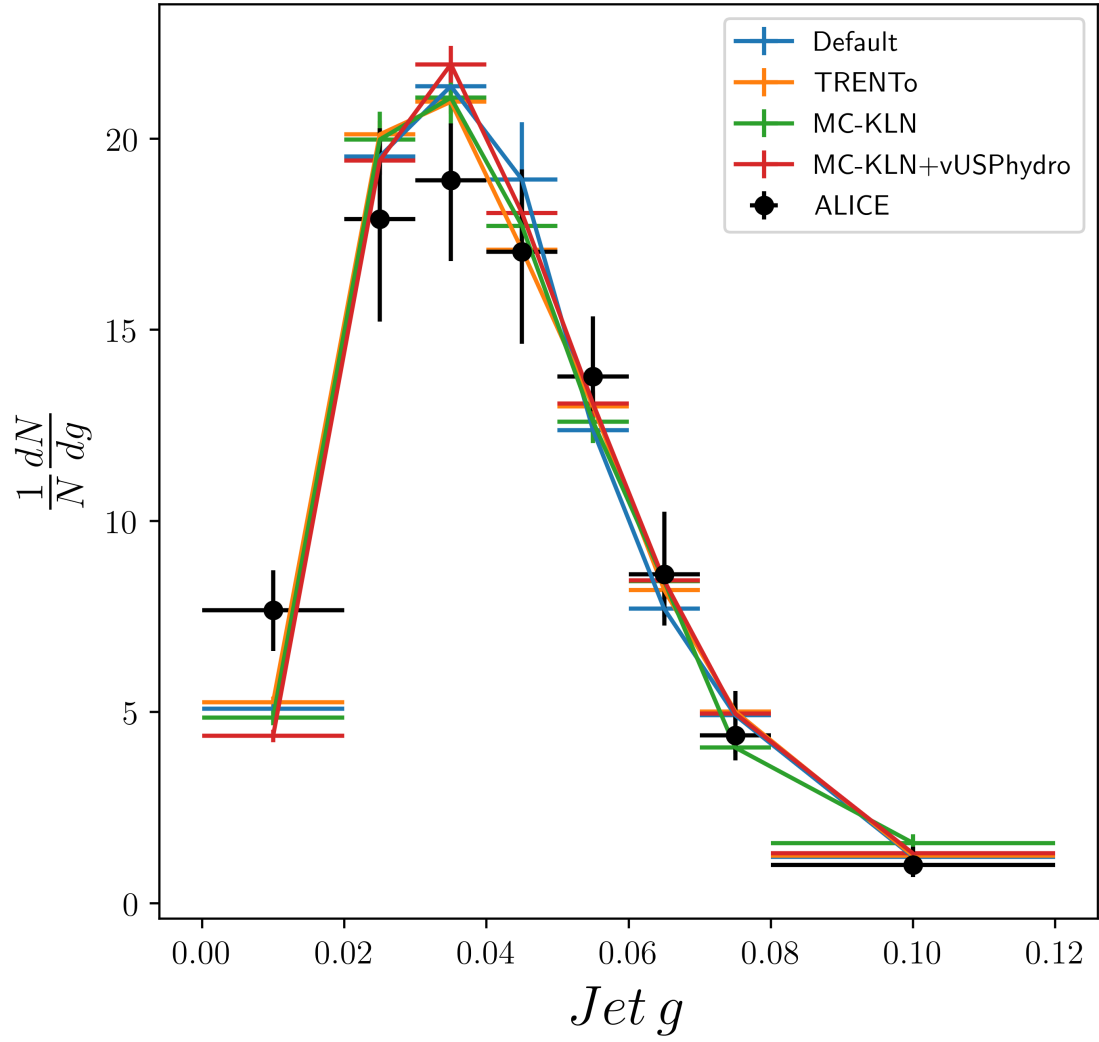


Figure 4.16: Jet Girth for charged jets calculated for $R = 0.2$ anti-kt algorithm and $|\eta| < 0.8$. $40\text{GeV}/c < p_T < 60\text{GeV}$. The CM energy is $\sqrt{s_{NN}} = 2.76\text{TeV}$. On the 0 – 10% centrality class.

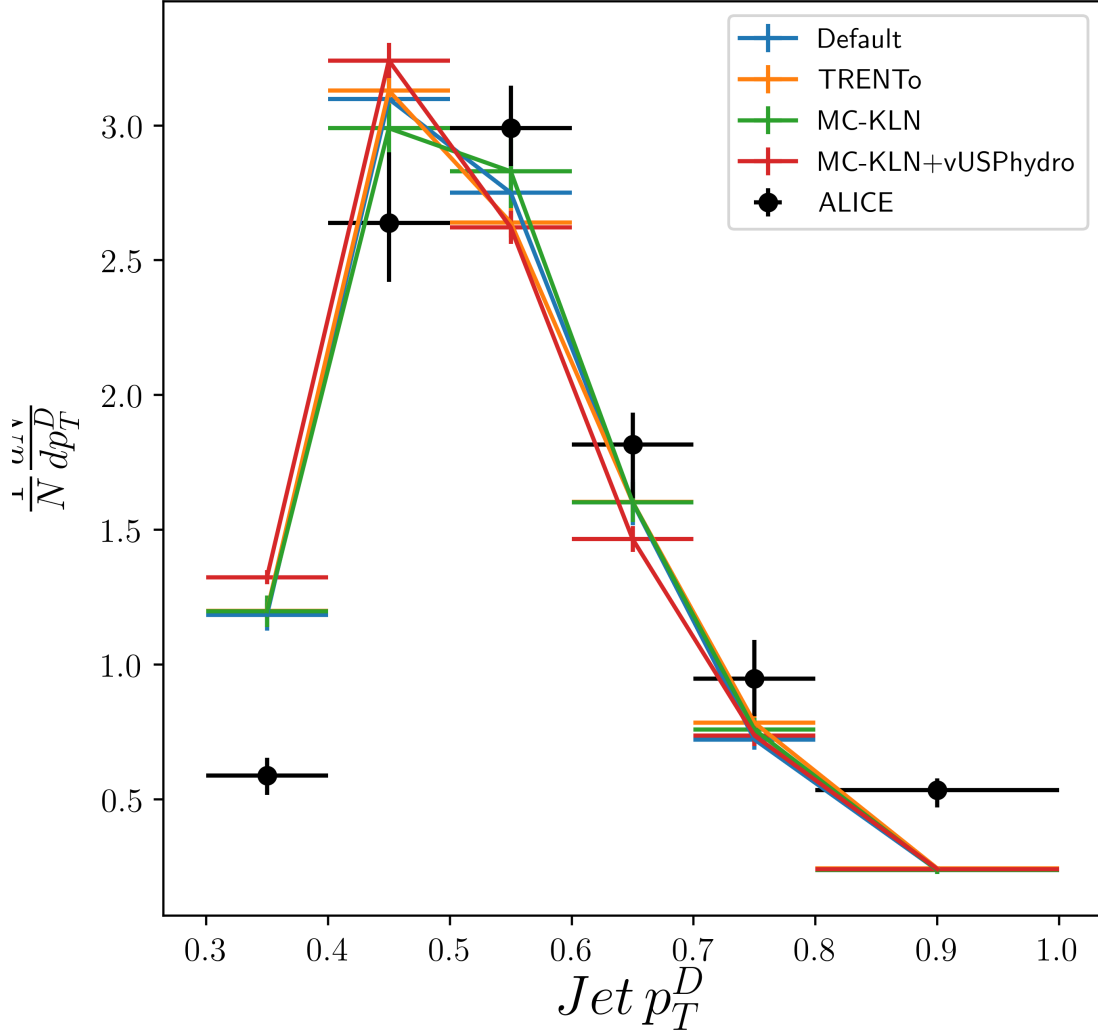


Figure 4.17: Jet Dispersion for charged jets calculated for $R = 0.2$ anti-kt algorithm and $|\eta| < 0.8$. $40\text{GeV}/c < p_T < 60\text{GeV}$. The CM energy is $\sqrt{s_{NN}} = 2.76\text{TeV}$. On the 0 – 10% centrality class.

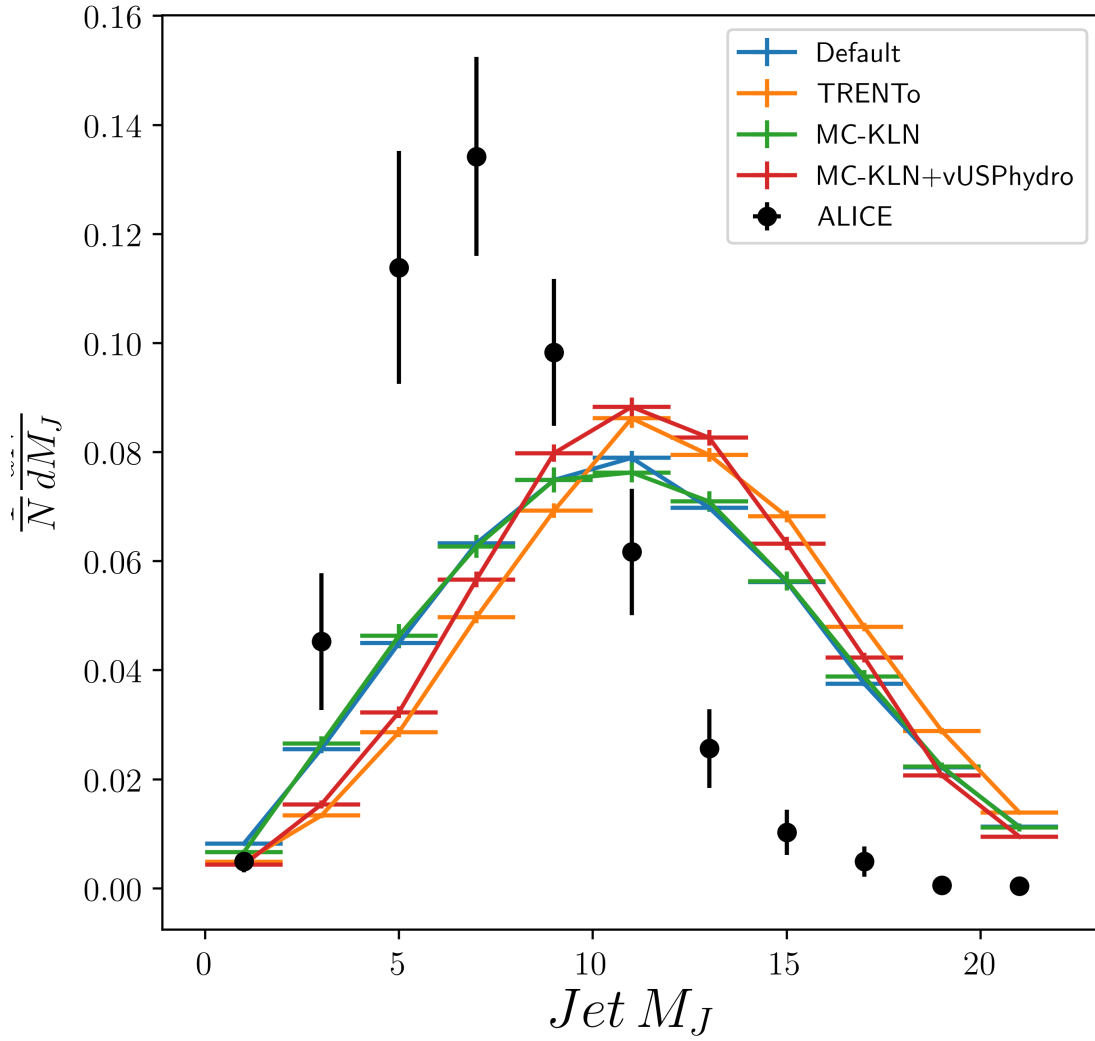


Figure 4.18: Jet Mass for charged jets calculated for $R = 0.2$ anti-kt algorithm and $|\eta| < 0.8$. $40\text{GeV}/c < p_T < 60\text{GeV}$. The CM energy is $\sqrt{s_{NN}} = 2.76\text{TeV}$. On the 0 – 10% centrality class.

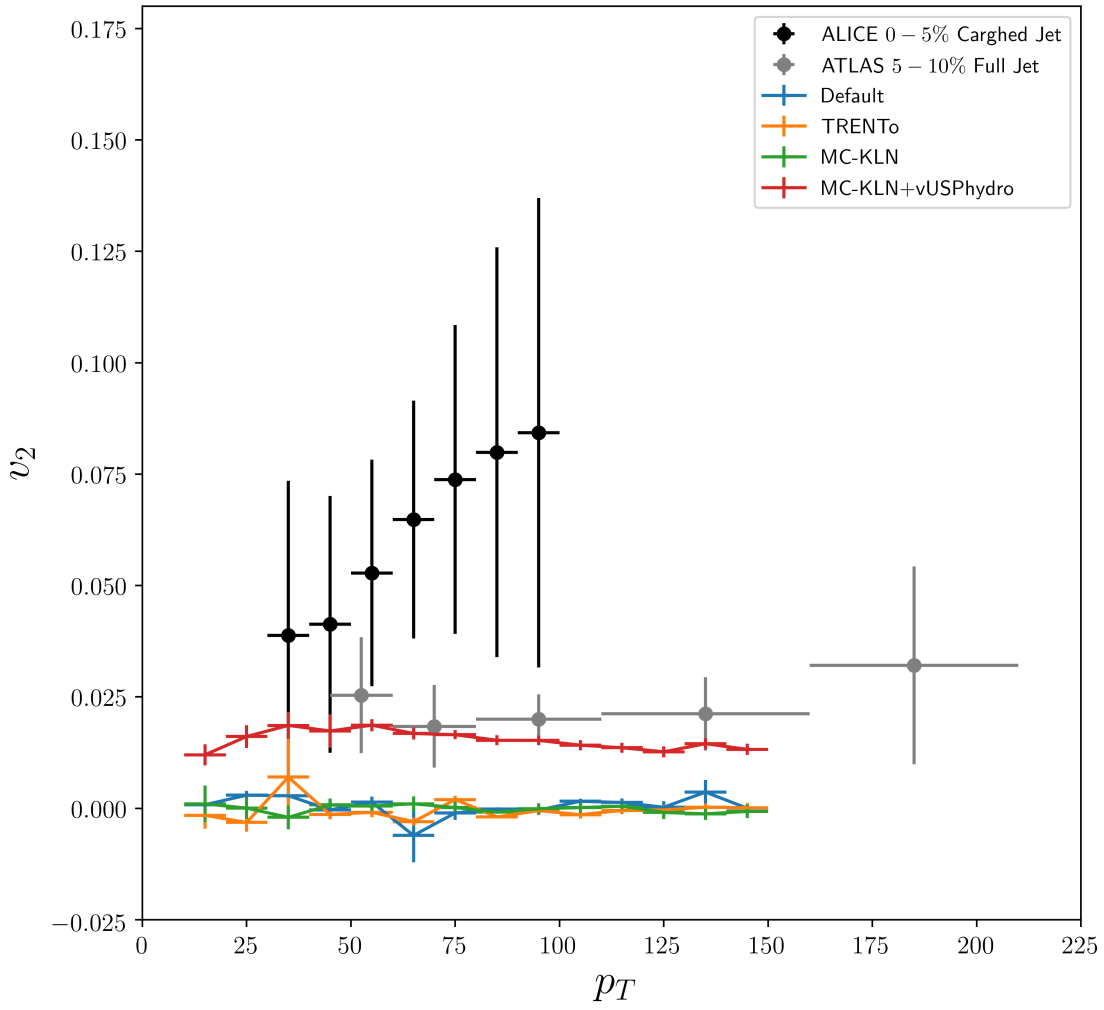


Figure 4.19: Jet v_2 calculated for $R = 0.4$ anti-kt algorithm and $|\eta| < 0.8$. The CM energy is $\sqrt{s_{NN}} = 2.76\text{TeV}$. On the 0 – 10% centrality class.

Chapter 5

Conclusion

The results presented in the previous chapter show that, as far as the jet structure and shape are concerned, there are no major modifications of the observables due to the inclusion of realistic hydro and initial conditions. Some improvements came on the jet mass, but only slightly.

To improve the description of the data, other things could be modified. First, there is still the hadronization mechanism that is used by JEWEL, which comes from PYTHIA. This mechanism is built to explain pp data. Jets formed in heavy-ion collisions might be substantially different due to their hadronization mechanism. Effects of coalescence might play a big role here, giving new color partners to the leading partons describing the jets.

Another thing that was not implemented in this work is the local four-velocity and a realistic EOS. This could further improve the description of the data. Since the partons are moving through the medium and the medium itself is most of the time moving outwards, the collisions could be more collinear than JEWEL default predicts. This could collimate the jet further, resulting in narrower jets. The collisions would be softer as well, since the CM of the local elastic collisions would be smaller, perhaps resulting in harder hadrons in the center of the jets in the final state. This could improve the p_T^D data as well.

The sample of the results presented in this work shows that there is not, as far as internal jet substructure and shape is concerned, a major improvement in describing the observables by implementing more realistic initial conditions or realistic hydrodynamics. Also, the correlation between medium and jets does present modifications due to the inclusion of a more realistic background, as indicated in the v_2 results. There is still high uncertainty in the experimental data, and further experimental improvement is needed for more detailed comparisons. The fact that this observable showed a value different from zero does indicate that high energy partons

can be used to investigate properties of the medium through this kind of observable. Further information can be potentially extracted from the medium by looking at higher moments of the Fourier decomposition. This can aid in constraining the models applied in these predictions, as well as extract the transport coefficients from the QGP.

Bibliography

- [1] F. Halzen and A. D. Martin, *QUARKS AND LEPTONS: AN INTRODUCTORY COURSE IN MODERN PARTICLE PHYSICS*. John Willey and Sons, 1984.
- [2] G. Dissertori, I. G. Knowles, J. C. H. Spence, and M. Schmelling, *Quantum Chromodynamics: High Energy Experiments and Theory*. Oxford University Press, 2003. Google-Books-ID: IRUxDgAAQBAJ.
- [3] T. D. Lee, “Abnormal nuclear states and vacuum excitation,” *Reviews of Modern Physics*, vol. 47, pp. 267–275, Apr. 1975.
- [4] M. E. Peskin and D. V. Schroeder, *An Introduction To Quantum Field Theory*. Avalon Publishing, Oct. 1995. Google-Books-ID: EVeNNcslvX0C.
- [5] E. Fermi, “High-energy nuclear events,” *Prog.Theor.Phys.*, vol. 5, pp. 570–583, 1950.
- [6] E. M. Lifshitz and L. D. Landau, “Statistical Physics, Part 1,” 1980.
- [7] D. T. Haar, *Collected Papers of L.D. Landau*. Elsevier, Oct. 2013. Google-Books-ID: epc4BQAAQBAJ.
- [8] J. Letessier and J. Rafelski, *Hadrons and QuarkGluon Plasma*. May 2002.
- [9] J. Adams *et al.*, “Experimental and theoretical challenges in the search for the quark gluon plasma: The STAR Collaboration’s critical assessment of the evidence from RHIC collisions,” *Nucl. Phys. A*, vol. 757, pp. 102–183, 2005.
- [10] E. Ferrer and V. Incera, “Exploring Dense and Cold QCD in Magnetic Fields,” *The European Physical Journal A*, vol. 52, Aug. 2016.
- [11] D. d’Enterria, “Jet quenching in QCD matter: from RHIC to LHC,” *Nuclear Physics A*, vol. 827, pp. 356c–364c, Aug. 2009.

- [12] J. D. Bjorken, “Highly relativistic nucleus-nucleus collisions: The central rapidity region,” *Physical Review D*, vol. 27, pp. 140–151, Jan. 1983.
- [13] K. Zapp, G. Ingelman, J. Rathsman, and J. Stachel, “Jet quenching from soft QCD scattering in the quark-gluon plasma,” *Phys.Lett.*, vol. B637, pp. 179–184, 2006.
- [14] W. Florkowski, *Phenomenology of Ultra-Relativistic Heavy-Ion Collisions*. World Scientific Publishing Company, Mar. 2010. Google-Books-ID: GhY8DQAAQBAJ.
- [15] P. Romatschke, “New Developments in Relativistic Viscous Hydrodynamics,” *International Journal of Modern Physics E*, vol. 19, pp. 1–53, Jan. 2010. arXiv: 0902.3663.
- [16] R. Scharenberg, B. Srivastava, A. Hirsch, and C. Pajares, “Hot Dense Matter: Deconfinement and Clustering of Color Sources in Nuclear Collisions,” *Universe*, vol. 4, p. 96, Sept. 2018.
- [17] M. L. Miller, K. Reygers, S. J. Sanders, and P. Steinberg, “Glauber Modeling in High Energy Nuclear Collisions,” *Annual Review of Nuclear and Particle Science*, vol. 57, pp. 205–243, Nov. 2007.
- [18] K. Zapp, G. Ingelman, J. Rathsman, J. Stachel, and U. A. Wiedemann, “A Monte Carlo Model for ‘Jet Quenching’,” *The European Physical Journal C*, vol. 60, pp. 617–632, Apr. 2009. arXiv: 0804.3568.
- [19] K. C. Zapp, J. Stachel, and U. A. Wiedemann, “A local Monte Carlo framework for coherent QCD parton energy loss,” *Journal of High Energy Physics*, vol. 2011, July 2011. arXiv: 1103.6252.
- [20] J. S. Moreland, J. E. Bernhard, and S. A. Bass, “Alternative ansatz to wounded nucleon and binary collision scaling in high-energy nuclear collisions,” *Phys.Rev.*, vol. C92, p. 011901, July 2015.
- [21] H.-J. Drescher and Y. Nara, “Effects of fluctuations on the initial eccentricity from the Color Glass Condensate in heavy ion collisions,” *Physical Review C*, vol. 75, p. 034905, Mar. 2007. arXiv: nucl-th/0611017.
- [22] Y. V. Kovchegov and E. Levin, *Quantum Chromodynamics at High Energy*. Cambridge University Press, Aug. 2012.

- [23] K. C. Zapp, F. Krauss, and U. A. Wiedemann, “A perturbative framework for jet quenching,” *Journal of High Energy Physics*, vol. 2013, Mar. 2013. arXiv: 1212.1599.
- [24] J. Noronha-Hostler, J. Noronha, and F. Grassi, “Bulk viscosity-driven suppression of shear viscosity effects on the flow harmonics at energies available at the BNL Relativistic Heavy Ion Collider,” *Physical Review C*, vol. 90, p. 034907, Sept. 2014.
- [25] J. Noronha-Hostler, G. S. Denicol, J. Noronha, R. P. G. Andrade, and F. Grassi, “Bulk Viscosity Effects in Event-by-Event Relativistic Hydrodynamics,” *Physical Review C*, vol. 88, Oct. 2013. arXiv: 1305.1981.
- [26] “Jacquelyn Noronha-Hostler | v-USPhydro.”
- [27] G. S. Denicol, T. Kodama, T. Koide, and P. Mota, “Effect of bulk viscosity on Elliptic Flow near QCD phase transition,” *Physical Review C*, vol. 80, p. 064901, Dec. 2009. arXiv: 0903.3595.
- [28] G. S. Denicol, T. Kodama, and T. Koide, “The effect of shear and bulk viscosities on elliptic flow,” *Journal of Physics G: Nuclear and Particle Physics*, vol. 37, p. 094040, Sept. 2010. arXiv: 1002.2394.
- [29] K. C. Zapp, “JEWEL 2.0.0 - Directions for Use,” *The European Physical Journal C*, vol. 74, Feb. 2014. arXiv: 1311.0048.
- [30] T. Sjostrand, S. Mrenna, and P. Skands, “PYTHIA 6.4 Physics and Manual,” *Journal of High Energy Physics*, vol. 2006, pp. 026–026, May 2006. arXiv: hep-ph/0603175.
- [31] C.-Y. Wong, *Introduction to High-energy Heavy-ion Collisions*. World Scientific, 1994. Google-Books-ID: Fnxvrdj2NOQC.
- [32] C. Bierlich, A. Buckley, J. M. Butterworth, L. Corpe, D. Grellscheid, C. Gutsche, P. Karaczmarczyk, J. Klein, L. Lonnblad, C. S. Pollard, H. Schulz, and F. Siegert, “Robust Independent Validation of Experiment and Theory: Rivet version 3,” *arXiv:1912.05451 [hep-ex, physics:hep-ph]*, Dec. 2019. arXiv: 1912.05451.
- [33] M. Cacciari, G. P. Salam, and G. Soyez, “FastJet user manual: (for version 3.0.2),” *The European Physical Journal C*, vol. 72, p. 1896, Mar. 2012.

-
- [34] K. C. Zapp, “Geometrical aspects of jet quenching in JEWEL,” *Physics Letters B*, vol. 735, pp. 157–163, July 2014. arXiv: 1312.5536.
 - [35] W. T. Vetterling and W. H. Press, *Numerical Recipes in FORTRAN: The Art of Scientific Computing*. Cambridge University Press, 1992. Google-Books-ID: ruR6ds7RIpEC.
 - [36] G. P. Salam, “Towards jetography,” *The European Physical Journal C*, vol. 67, pp. 637–686, June 2010.
 - [37] A. Collaboration, “Measurement of jet suppression in central Pb-Pb collisions at $\sqrt{s_{\rm NN}} = 2.76$ TeV,” *Physics Letters B*, vol. 746, pp. 1–14, June 2015. arXiv: 1502.01689.
 - [38] M. Connors, C. Nattrass, R. Reed, and S. Salur, “Review of Jet Measurements in Heavy Ion Collisions,” *arXiv:1705.01974 [nucl-ex]*, May 2017.
 - [39] A. Collaboration, “Medium modification of the shape of small-radius jets in central Pb-Pb collisions at $\sqrt{s_{\rm NN}} = 2.76$, \rm{TeV} ,” *arXiv:1807.06854 [hep-ex, physics:nucl-ex]*, July 2018. arXiv: 1807.06854.
 - [40] A. Collaboration, “First measurement of jet mass in Pb-Pb and p-Pb collisions at the LHC,” *Physics Letters B*, vol. 776, pp. 249–264, Jan. 2018. arXiv: 1702.00804.
 - [41] R. K. Elayavalli and K. C. Zapp, “Medium response in JEWEL and its impact on jet shape observables in heavy ion collisions,” *Journal of High Energy Physics*, vol. 2017, July 2017. arXiv: 1707.01539.

Index

R_{AA} , 7

anysotropic flow, 7

asymptotic freedom, 5, 8

conservation equation, 9

coupling constant, 5

critical temperature, 8

Jet

 Quenching, 8

mass spectrum, 6

model

 Hagedorn, 6

perturbation theory, 5

prescription

 Cooper-Frye, 9

strangeness, 7

 enhancement, 7

Strong Force, 5